NAVAL POSTGRADUATE SCHOOL

MONTEREY, CALIFORNIA

THESIS

QUANTIFYING FACTORS AFFECTING OPTICAL TURBULENCE PROPAGATION USING A CONTROLLED TOWED VEHICLE FROM AN AIRCRAFT

by

Alonzo Ingram Jr.

December 2017

Thesis Advisor:	Qing Wang
Second Reader:	Peter Guest

Approved for public release. Distribution is unlimited.

THIS PAGE INTENTIONALLY LEFT BLANK

REPORT DOCUMENTATION PAGE	Form Approved OMB No. 0704-0188

Public reporting burden for this collection of information is estimated to average 1 hour per response, including the time for reviewing instructions, searching existing data sources, gathering and maintaining the data needed, and completing and reviewing the collection of information. Send comments regarding this burden estimate or any other aspect of this collection of information, including suggestions for reducing this burden, to Washington Headquarters Services, Directorate for Information Operations and Reports, 1215 Jefferson Davis Highway, Suite 1204, Arlington, VA 22202-4302, and to the Office of Management and Budget, Paperwork Reduction Project (0704-0188) Washington, DC 20503.

1. AGENCY USE ONLY *(Leave blank)*	2. REPORT DATE December 2017	3. REPORT TYPE AND DATES COVERED Master's thesis

4. TITLE AND SUBTITLE QUANTIFYING FACTORS AFFECTING OPTICAL TURBULENCE PROPAGATION USING A CONTROLLED TOWED VEHICLE FROM AN AIRCRAFT	5. FUNDING NUMBERS
6. AUTHOR(S) Alonzo Ingram Jr.	
7. PERFORMING ORGANIZATION NAME(S) AND ADDRESS(ES) Naval Postgraduate School Monterey, CA 93943-5000	8. PERFORMING ORGANIZATION REPORT NUMBER
9. SPONSORING /MONITORING AGENCY NAME(S) AND ADDRESS(ES) N/A	10. SPONSORING / MONITORING AGENCY REPORT NUMBER

11. SUPPLEMENTARY NOTES The views expressed in this thesis are those of the author and do not reflect the official policy or position of the Department of Defense or the U.S. Government. IRB number ____N/A____.

12a. DISTRIBUTION / AVAILABILITY STATEMENT Approved for public release. Distribution is unlimited.	12b. DISTRIBUTION CODE A

13. ABSTRACT (maximum 200 words)

High Energy Laser (HEL) systems are advantageous for their precision against small surface targets, lethality, and ability to deliver power. Yet their performances are impacted by atmospheric turbulence and aerosols. It is thus crucial to quantify such atmospheric effects to aid the optical system design and/or to predict their operational conditions. The main objective of this study is to quantify optical turbulence in the marine atmospheric boundary layer that impacts ship-based optical systems. I utilized measurements from the Coupled Air Sea Processes and Electromagnetic Ducting Research (CASPER) East field campaign. In particular, the Controlled Towed Vehicle (CTV) tethered to the CIRPAS Twin Otter research aircraft was analyzed for horizontal and vertical variabilities of the structure function parameter, C_n^2, and the associated components of temperature, humidity, and the cross-correlation between the two. I identified the predominant contributions of temperature perturbations to C_n^2 similar to that over land. The effects of water vapor are negligibly small. However, temperature and humidity correlations can contribute 20% of the total C_n^2 in unstable conditions. In stable conditions, this term becomes consistently negative. The dependence of C_n^2 on wind speed and thermal stability was illustrated using individual examples as well as all available data.

14. SUBJECT TERMS Scintillation, C_n^2, Controlled Towed Vehicle (CTV), CASPER-East, air-sea temperature difference (*ASTD*), thermo-stability, High-Energy Laser (HEL), Electromagnetic (EM), Electro-Optical (EO)	15. NUMBER OF PAGES 67
	16. PRICE CODE

17. SECURITY CLASSIFICATION OF REPORT	18. SECURITY CLASSIFICATION OF THIS PAGE	19. SECURITY CLASSIFICATION OF ABSTRACT	20. LIMITATION OF ABSTRACT
Unclassified	Unclassified	Unclassified	UU

NSN 7540-01-280-5500 Standard Form 298 (Rev. 2-89) Prescribed by ANSI Std. 239-18

THIS PAGE INTENTIONALLY LEFT BLANK

Approved for public release. Distribution is unlimited.

QUANTIFYING FACTORS AFFECTING OPTICAL TURBULENCE PROPAGATION USING A CONTROLLED TOWED VEHICLE FROM AN AIRCRAFT

Alonzo Ingram Jr.
Lieutenant, United States Navy
B.A., Thomas Edison State University, 2011

Submitted in partial fulfillment of the
requirements for the degree of

**MASTER OF SCIENCE IN METEOROLOGY
AND PHYSICAL OCEANOGRAPHY**

from the

**NAVAL POSTGRADUATE SCHOOL
December 2017**

Approved by: Dr. Qing Wang
Thesis Advisor

Dr. Peter Guest
Second Reader

Dr. Wendell Nuss
Chair, Department of Meteorology

THIS PAGE INTENTIONALLY LEFT BLANK

ABSTRACT

High Energy Laser (HEL) systems are advantageous for their precision against small surface targets, lethality, and ability to deliver power. Yet their performances are impacted by atmospheric turbulence and aerosols. It is thus crucial to quantify such atmospheric effects to aid the optical system design and/or to predict their operational conditions. The main objective of this study is to quantify optical turbulence in the marine atmospheric boundary layer that impacts ship-based optical systems. I utilized measurements from the Coupled Air Sea Processes and Electromagnetic Ducting Research (CASPER) East field campaign. In particular, the Controlled Towed Vehicle (CTV) tethered to the CIRPAS Twin Otter research aircraft was analyzed for horizontal and vertical variabilities of the structure function parameter, C_n^2, and the associated components of temperature, humidity, and the cross-correlation between the two. I identified the predominant contributions of temperature perturbations to C_n^2 similar to that over land. The effects of water vapor are negligibly small. However, temperature and humidity correlations can contribute 20% of the total C_n^2 in unstable conditions. In stable conditions, this term becomes consistently negative. The dependence of C_n^2 on wind speed and thermal stability was illustrated using individual examples as well as all available data.

THIS PAGE INTENTIONALLY LEFT BLANK

TABLE OF CONTENTS

I. INTRODUCTION 1
- A. OVERVIEW 1
- B. OBJECTIVES OF THE THESIS 2
- C. MILITARY APPLICATION 3
- D. STRUCTURE OF THE THESIS 4

II. BACKGROUND 5
- A. ATMOSPHERIC EFFECTS ON SHORTWAVE AND OPTICAL PROPAGATION 5
  - 1. Scintillation 6
  - 2. Beam Spreading 9
  - 3. Beam Wander 9
  - 4. Absorption and Scattering 10
  - 5. Thermal Blooming 10
- B. VARIABLES TO DESCRIBE SCINTILLATION 11
- C. SCINTILLATION (C_N^2) MODELS 12
  - 1. NSLOT 13
  - 2. NAVSLaM 13
  - 3. Hufnagel-Valley Model 13
  - 4. PAMELA Model 14
  - 5. HELCAP 14
  - 6. Wave-Train 14
  - 7. Wave-Prop 15
- D. OPTICAL SYSTEMS—SENSORS AND HEL WEAPONS USAGE 15

III. DATA COLLECTION AND METHODOLOGY 17
- A. CASPER-EAST FIELD CAMPAIGN 17
- B. AIRCRAFT MEASUREMENTS FROM CASPER-EAST 19
  - 1. CIRPAS Twin Otter 20
  - 2. Controlled Towed Vehicle 21
- C. CASPER-EAST CTV DATA PROCESSING 23

IV. DATA ANALYSES AND RESULTS 25
- A. SELECTION OF DATA SECTIONS 25
- B. HORIZONTAL VARIATIONS 30
- C. VERTICAL VARIATIONS 37

D. EFFECTS OF WIND AND THERMAL STABILITY 42

V. SUMMARY AND CONCLUSION 45

LIST OF REFERENCES 47

INITIAL DISTRIBUTION LIST 51

LIST OF FIGURES

Figure 1. Atmospheric Effects on Shortwave and Optical Propagation: Impacting a Soldier's Ability to Target a Distant Object. Adapted from Koretsky (2013). 6

Figure 2. Example of Astronomical Scintillation. Source: Redorbit (2017). 7

Figure 3. Example of Unstable Atmosphere Defocusing a Laser Beam Wavefront. Adapted from Burger et al. (2008).....8

Figure 4. Comparison of Turbulent Cell Size with Beam Wander and Scintillation. Adapted from Alkholidi and Altowij (2014).....10

Figure 5. U.S. Army Corps of Engineers Field Research Facility Pier, Duck, North Carolina. Source: Field Research Facility (1992). 18

Figure 6. Data Collection Platforms Used for CASPER East Field Campaign. Source: Wang (2017). 19

Figure 7. CIRPAS Twin Otter Towing Controlled Towed Vehicle below for Data Collection. Source: Khelif (2013). 20

Figure 8. CIRPAS Twin Otter Instrumentation Setup Used for the Unified Physical Parameterization for Extended Forecast. Adapted from Khelif (2013).....21

Figure 9. CIRPAS Controlled Towed Vehicle Mounted to the Twin Otter before Deployment (top left), Instrument Locations Seen from Outside (top right) and Inside (lower panel). Adapted from Khelif (2016).....22

Figure 10. Flight Tracks of all Twin Otter Flights during CASPER-East. Adapted from Khelif (2016). 23

Figure 11. A Three-Dimensional View of an Example Flight Path of TO/CTV during CASPER-East. Source: Khelif (2016).....23

Figure 12. An Example of Selection of Useful Data Sections 26

Figure 13. Illustrations of the Data Sections Chosen for Analyses to Reveal Vertical and Horizontal Variabilities 27

Figure 14. Horizontal Variations of Boundary Layer Mean, Turbulence, and Optical Turbulence Properties Calculated Based on Measurements from Leg 8 at 11 m above Sea Level on 17 October 2015 31

Figure 15. Same as Figure 14, Except for Leg 10 at 12 m above Sea Level on 31 October 2015 32

Figure 16. Same as Figure 14, Except for Leg 2 at 11 m above Sea Level on 27 October 2015 34

Figure 17. Same as Figure 14, Except for Leg 9 at 12 m above Sea Level on 01 November 2015 36

Figure 18. Vertical Variations of Mean and Optical Turbulence Properties Observed from Legs 6–11 on 14 October 2015 39

Figure 19. Same as Figure 18, Except for Legs 1–5 on 16 October 2015, over the Shelf Region 40

Figure 20. Same as Figure 18, Except for Legs 12–15 on 31 October 2015, over the Gulf Stream 41

Figure 21. Effects of Wind Speed on C_n^2 and its Components 42

Figure 22. Same as Figure 21, Except for Variation with *ASTD* 43

LIST OF TABLES

Table 1. Summary of CASPER-East Flight and Selected Data Legs for Different Types of Analyses 29

THIS PAGE INTENTIONALLY LEFT BLANK

LIST OF ACRONYMS AND ABBREVIATIONS

ABL	Atmospheric Boundary Layer
ASL	Above Sea Level
CASPER	Coupled Air Sea Processes and Electromagnetic Ducting Research
CIRPAS	Center for Interdisciplinary Remote Piloted Aircraft Study
CTV	Controlled Towed Vehicle
DE	Directed Energy
EM	Electromagnetic
EO	Electro-Optical
GS	Gulf Stream
HEL	High-Energy Laser
HELCAP	High-Energy Laser Code for Atmospheric Propagation
IR	Infrared
LHR	Laser Heterodyne Radiometer
LWR	Laser Warning Receiver
MASL	Marine Atmospheric Surface Layer
MOST	Monin-Obukhov Similarity Theory
NAVSLaM	Navy Atmospheric Vertical Surface Layer Model
NPS	Naval Postgraduate School
NSLOT	Navy Surface Layer Optical Turbulence
NWP	Numerical Weather Predictions
ONR	Office of Naval Research
OTG	Optical Turbulence Generating
OTL	Optical Targeting Lasers
TO	Twin Otter
UAV	Unmanned Aerial Vehicle

THIS PAGE INTENTIONALLY LEFT BLANK

I. INTRODUCTION

A. OVERVIEW

The utilization of laser weapons on the battlefield is of vital importance to future military operations and is the central focus of the Department of Defense (DOD)-directed energy research program. Laser weapons deliver power and lethality with precision to small surface targets and many air platforms, such as unmanned aerial vehicles (UAVs). They have been shown to provide a highly efficient and affordable defense capability using High Energy Laser (HEL) systems. This thesis will quantify how temperature and water vapor contribute to maritime shortwave terrestrial scintillation by using measurements from the Controlled Towed Vehicle (CTV) tethered from the Twin Otter research aircraft during the Coupled Air Sea Processes and Electromagnetic Ducting Research (CASPER)-East Coast Field Campaign.

The study of HEL beam propagation is crucial for the development and execution of a comprehensive investment strategy for laser weapons. HELs are "concentrations of high-intensity visible light beams with hundreds of kilowatts to megawatts of average power" in a given direction (Coffey 2014). In the past fifty years, the U.S. military has engaged in developing HEL technology to gain a tactical advantage on the battlefield. Since 2000, the U.S. High Energy Laser Joint Technology Office (HEL-JTO) has supported university research programs on all aspects of the HEL system development. Sponsered topics include "the fundamental research of technologies that lead to the next generation of HELs and laser systems, advanced beam control, and better representation of Earth's lower atmosphere" (Seeley and Slater 2004).

The earth's gaseous atmosphere contains 78% nitrogen, 21% oxygen, 0.9% argon, and 0.03% carbon dioxide and water vapor (Angelo 2009). There are also small particles such as dust, sea salts, and other natural or anthropogenic particles, all referred to as aerosols, in the atmosphere. All components of the atmosphere attenuate and redirect the HEL beam by scattering and absorption of the visible radiation. Meanwhile, atmospheric turbulence results in fluctuations of apparent brightness which is normally referred to as

atmospheric scintillation, "leading to beam spreading, beam wander (or steering), and the loss of spatial and temporal coherence" (Sprangle et al. 2007).

Therefore, propagation of HEL energy through the atmospheric medium needs to be quantified accurately in order to predict the effectiveness of the laser beam on targets, improve test planning, and help direct the deployment of high energy laser systems. Understanding and mitigating the impact of the atmosphere on HEL system is thus also a crucial part of HEL weapon research. Unfortunately, current atmospheric models do not accurately represent the lower atmosphere variable constituents such as water vapor and aerosol concentrations. The prediction of the atmospheric turbulence, particularly in the lowest 100 meters, also has large uncertainties.

B. OBJECTIVES OF THE THESIS

The impact of the atmosphere on HEL systems varies significantly in time and space. Air motions like atmospheric turbulent eddies cause, "random fluctuations in the refractive index of air which produce phenomenon commonly referred to as optical turbulence" (Koretsky 2013). We can quantify the effects of optical turbulence on Electro-Optical (EO) propagation by using the structure-function parameters, C_T^2, C_{eT}, and C_e^2 (defined later). Past research has proven that, "the structure function parameters are proportional to the magnitude of the humidity and temperature spectra in the inertial sub-range" (Wesely 1976). As shown by a more recent study (Wyngaard and Kosovic 1994) these, "spectral levels are solely dependent on 'molecular destruction rates' of kinetic energy, temperature variations, and varying humidity plus their covariance." Similarly, Burk (1979) agrees with Wesely by affirming, "this type of relationship of function with optical C_n^2 is more determined by C_T^2." Equally for optical wavelengths, optical turbulence is due primarily to random temperature (and consequently density) fluctuations; though in certain cases humidity fluctuations can become important as well.

The refractive index structure parameter as quantified by C_n^2 "is the single most important parameter for quantifying the statistically-averaged impact of optical turbulence on laser beam quality" (Tatarskii 1971). C_n^2 appears in the equations describing scintillation (random intensity fluctuations), beam wander, beam spread, and

parameters such as Fried's coherence length (Sprangle et al. 2007). All the mentioned (C_n^2-dependent) effects of optical turbulence distort and diffuse a laser beam as it propagates through the atmosphere and reduces the focused laser energy that is delivered on a target. Without correction, the images viewed from telescopes in the vertical, or from rifle scopes in the horizontal suffer a loss of resolution of images because of optical turbulence. Frehlich (2010) used area-averaged estimates of C_n^2 from high-resolution numerical weather prediction (NWP) model output in field applications of meteorological model predictions; the conclusion was that the model output require improvements for the future. It is practical to compare measurements of optical turbulence with theoretical forecasts, and C_n^2 as the parameter that describes the scintillation effects on the HEL systems in all-optical propagation models (Wyngaard and Thomson 1993). Current atmospheric models of C_n^2 for HEL application derive from a limited number of field measurements. Their adequacy for broad applications needs to be tested using more observations. This thesis work will focus on C_n^2 variability in the lower atmosphere using in-situ aircraft measurements. This atmospheric structure function parameter quantifies the variability of temperature on the small scales that effect HEL system performance. The measured C_n^2 will be used to evaluate existing C_n^2 models and develop improvements, which is the ultimate goal of this thesis work.

C. MILITARY APPLICATION

The DOD needs to quantify, understand, and predict atmospheric effects on HEL propagation. HELs are applied in Laser Warning Receivers (LWR), target marking, missile defense, guiding munitions, and used as alternatives to radar and troop blinding. They are also operational in targeting the enemy (Coffey 2014). U.S. Naval platforms and sensors rely on the most advanced technologies to operate above, below, and in the air-sea boundary layer to support current operations. High Energy Lasers have proved efficiency in military actions. They are predicted to have broad applications in future military engagements as they receive more funding in comparison with other government departments as they provide a minimum "shot-to-shot" cost in operations (Coffey 2014). Taking a big step forward, the Navy tested its first ship-mounted Laser Weapon System (LaWS) in August 2014 aboard the USS PONCE, an amphibious transport ship. The

LaWS proved successful and was authorized as part of the ship's defensive weapon system two months later (Lendon 2014). The skill of quantifying the atmospheric impact on HEL beam still lags. There is a lack of knowledge about the behavior of C_n^2 under various atmospheric and surface forcing. There is also a lack of a comprehensive data-set to accurately test model depiction/prediction of C_n^2 and HEL system performance. This thesis work is an attempt to address these critical issues.

D. STRUCTURE OF THE THESIS

Chapter I gave a brief overview as to the importance of this research and introduced atmospheric effects on shortwave propagation, optical sensors, and HEL weapons. It also outlined the objectives of this writing and provide military applications for the research. Chapter II discusses amplified background information on the atmospheric effects on optical propagation. It also details the variables used to describe terrestrial scintillation affects, scintillation models, and optical performance models and uses. Chapter III introduces the CASPER-East Field Campaign and observed data-sets from the Twin Otter and Controlled Towed Vehicle aircrafts. In Chapter IV, the data processing and results are discussed. Moreover, the summary and conclusions in Chapter V also include recommendations for future work.

II. BACKGROUND

A. ATMOSPHERIC EFFECTS ON SHORTWAVE AND OPTICAL PROPAGATION

Scientific studies have proven that, "HEL propagation can be strongly affected by parameters of the atmospheric environment" (Sprangle et al. 2007) which can vary significantly depending on location and time. Sprangle et al. (2005) previously examined that the, "inter-related physical properties such as aerosol and molecular scattering, thermal scattering due to heated aerosols, and aerosol heating and vaporization can change the optimum wavelength for efficient HEL propagation." These aerosols consist of "hygroscopic" and "non-hygroscopic" suspended particles in different sizes. Hygroscopic aerosols absorb laser energy which is directed to the heating and vaporization of aerosol particles. However, the scattering and absorption of aerosols in the atmosphere depends on the radius of the aerosol particle -and vaporizing it increases the propagation. Non-hygroscopic aerosols, which include dust, are characterized by large absorption and scattering rates which are never vaporized by directed energy applications. They, therefore, heat the surrounding area thus causing shortwave propagation or thermal blooming (Sprangle et al. 2007), which will be discussed later.

An optical wave that propagates through the atmosphere will experience a variety of deleterious effects relevant to optical communication systems, laser systems, and imaging (Andrews 2004). Atmospheric phenomena and compositions such as turbulence, water droplets in rain and fog, aerosol particles in haze and pollution, etc., are factors that affect our ability to see remote objects.

Figure 1 illustrates how these factors can impact a soldier's ability to target remote objects. The black circles represent atmospheric gases and particles.

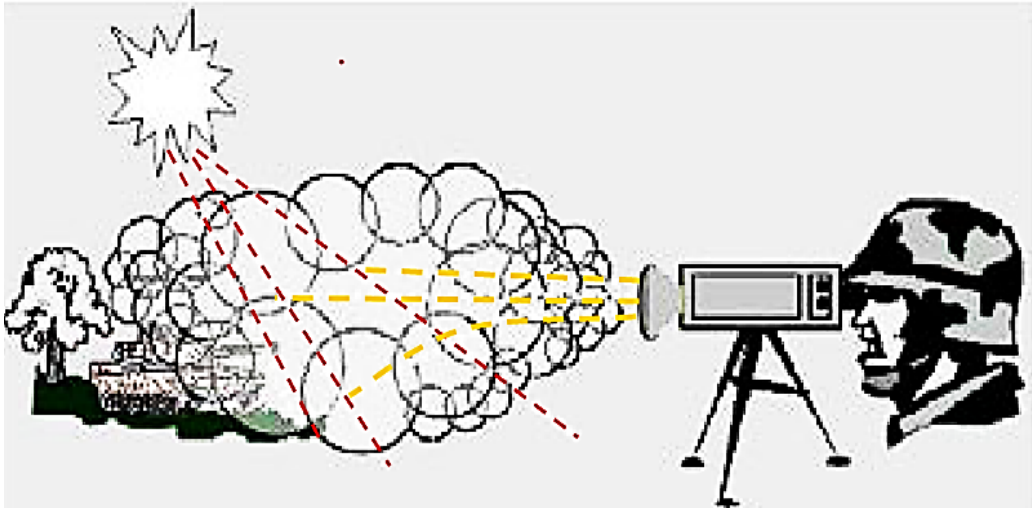

The scattering of light (yellow dashed lines) degrades apparent target depiction into the path between target and sensor. "This depends on aerosols and other particulates present, as well as any other potential sources of scattering, and it is particularly sensitive to the relative position of the Sun, target, and sensor" (Koretsky 2013).

Figure 1. Atmospheric Effects on Shortwave and Optical Propagation: Impacting a Soldier's Ability to Target a Distant Object. Adapted from Koretsky (2013).

Atmospheric turbulence, gas and particle composition cause optical processes such as scintillation, atmospheric absorption/scattering, beam spread, and beam wander (Andrews 2004). These processes represent the interaction between the optical beam and the atmosphere, and they substantially affect the performance of EO/IR sensors and HELs Weapon Systems operating in the atmosphere. These effects need to be quantified for the future development of such sensors and weapon systems.

1. Scintillation

Scintillation refers to "the temporal or spatial fluctuations in the irradiance of an optical wave caused by small fluctuations of the index of refraction" (Andrews 2004). These affect shortwave propagation by delaying frequency signals, refraction, and other effects. For those concerned with the coherent propagation of optical radiation, these fluctuations in the received irradiance of an optical system can be troublesome.

Past studies of atmospheric scintillation were associated with astronomical observations. "Light passing through the atmosphere passes through different regions

and conditions which have different refractive indices" (Chu 2001). Figure 2 illustrates how scintillation may affect the appearance of distant stars.

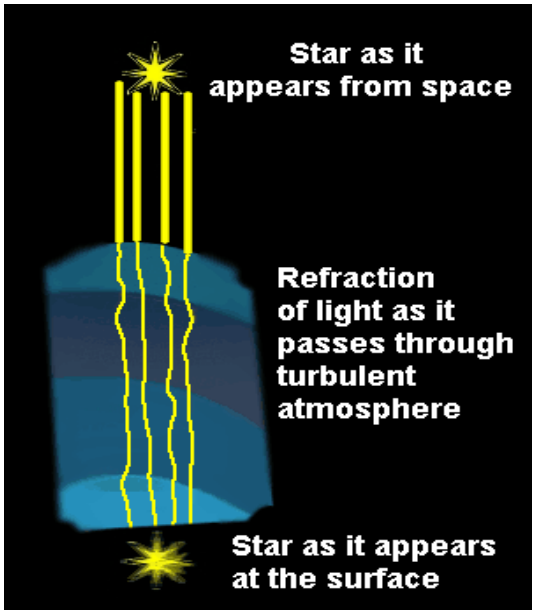

"Scintillation is a generic term for rapid variations in apparent position, brightness, or color of a distant luminous object viewed through the atmosphere. It is recognized that scintillation effects are caused by anomalous refractions occurring in rather small parcels, whose temperatures and densities differ slightly from those of their surroundings" (Pedrick 2004).

Figure 2. Example of Astronomical Scintillation. Source: Redorbit (2017).

As the visible light travels through the atmosphere, the wavefront is distorted, fluctuations alter and scatter electromagnetic radiation. Scintillation is why stars twinkle when seen from the surface of the Earth; as the starlight travels through the layers of the atmosphere. The stars seen from space appears much more focused compared to its distorted appearance at the surface.

Scintillation also affects optical sensors and HEL weapons in similar ways as its effects on astronomical observations. Scintillation in a fully turbulent environment is illustrated in Figure 3. As the laser beams pass through a turbulent atmosphere, terrestrial scintillation is introduced which causes optical images to become blurred and HEL weapons to degraded in their focus when reaching the target. The turbulence causes the

laser beam to spread and wander transversely (Sprangle et al. 2007). For example, images viewed from telescopes suffer a loss of resolution of images because of atmospheric refractive conditions. This is because fluctuations distort and scatter radiations of electromagnetic nature and sound waves. They have created urgency for comprehension of how the detailed "boundary structure" affects the response of sensors (Burk 1979). These refractive conditions are commonly used in field applications of meteorological model predictions, and they require improvement for the future.

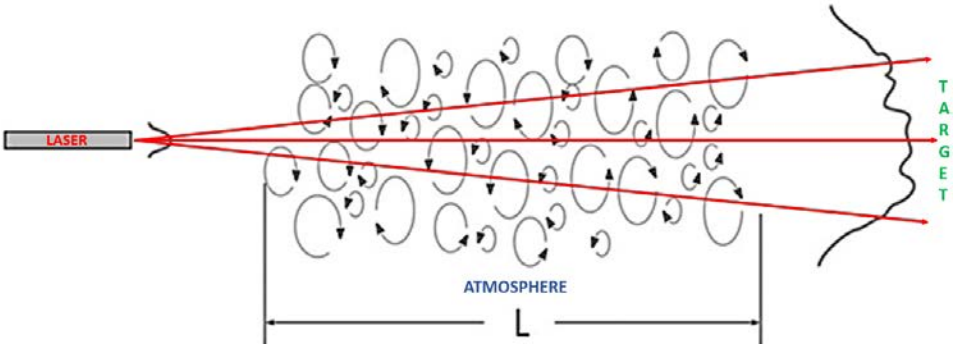

A focused laser beam (red lines) propagating through the atmosphere spreads due to diffraction but is influenced by turbulence in the form of randomly varying eddies (black circles). This causes the laser beam to defocus and spread some distance away from the target and lose power intensity.

Figure 3. Example of Unstable Atmosphere Defocusing a Laser Beam Wavefront. Adapted from Burger et al. (2008).

Although negatively impacting optical systems, scintillation effects can be used to obtain remote sounding of the turbulent atmospheric fields (Burk 1979). Many studies have attempted to relate the measured scintillation with the atmospheric parameters that contribute to the integrated scintillation over the path of propagation (McJannet et al. 2011, Benito et al. 2012). Because of these studies, terrestrial scintillation measurements can be used to derive turbulent sensible heat flux.

2. Beam Spreading

Beam spreading is a process laser beams experience as focused energy diffracts outward beyond ordinary deflection. From Andrews (2004) study, "this causes a power reduction at the receiver and/or distant target." The illustration in Figure 3 also shows how the energy from a laser, which is confined to a rather narrow cone, slowly diverges and spreads out as the distance increases. "Beam divergence is the angular measurement of growth in the radius with distance from the optical aperture as the beam emerges" (Andrews 2004). This generates the laser beam's spot size, which is nothing but the radius of the beam itself. For HEL weapon systems, the change in the spot size determines the average laser power on the target. The intensity of power may decrease due to transverse spreading and various processes, e.g., atmospheric turbulence and scattering events (Sprangle et al. 2007).

3. Beam Wander

Illustrated in Figure 4, beam wander is experienced when a laser beam changes in direction because of large turbulent eddies. Andrews (2004) states, if the size of the turbulence eddies is greater than the beam diameter the whole laser beam bends which leads to a displacement of the beam completely thus, causing erroneous target detection.

The effects of beam spreads and beam wander for larger scale turbulence eddies are similar in that they do not influence small fluctuations and negative peak as do scintillation. However, their importance is in the attainment of high-resolution numerical weather prediction technology (Frehlich et al. 2010). Figure 4 shows the desired beam path, from the laser source to the detector.

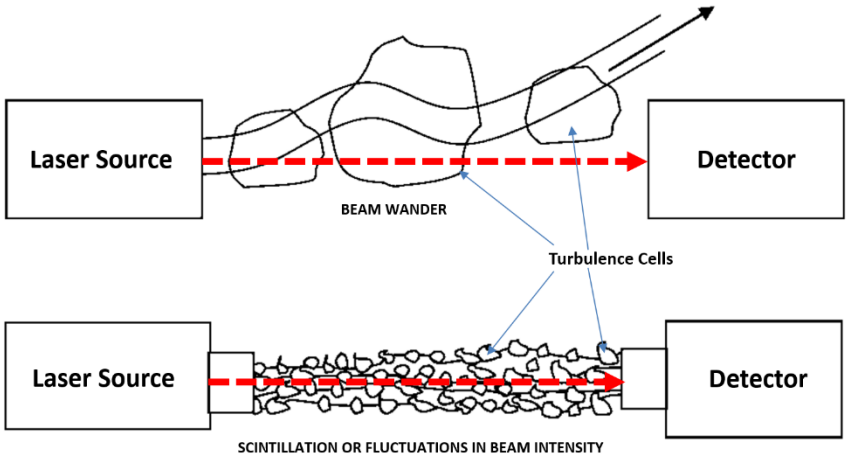

Top—Laser Beam Wander due to "turbulence cells that are larger than the beam diameter" (Alkholidi and Altowij 2014). Bottom - Scintillation or fluctuations in beam intensity at the receiver due to "turbulence cells that is smaller than the beam diameter" (Alkholidi and Altowij 2014). Red dashed lines represent the ideal energy path. Blue arrows point to varying turbulent cell sizes.

Figure 4. Comparison of Turbulent Cell Size with Beam Wander and Scintillation. Adapted from Alkholidi and Altowij (2014).

4. Absorption and Scattering

Atmospheric absorption and scattering involve the absorption or redirection of radiative energy by gas and aerosol particles. The most important gas molecules that absorb and emit radiative energy in the visible wavelength are water vapor and carbon dioxide, although all gas molecules cause scattering of the radiative energy, particularly in the short wavelength (Myron B. Thompson Academy 2006). Aerosols scatter or absorb sunlight to various degrees. These particles can be found in or over the ocean, mountains, forests, and deserts (Sprangle et al. 2007). They regulate the intensity and spread of the laser energy as it is directed to the target. Aerosol scattering and absorption are the key factors affecting optical imaging, target detection, and HEL system performances.

5. Thermal Blooming

Thermal blooming is another adverse atmospheric effect that affects HEL system performance. It is three-dimensional and time-dependent and causes laser beams to defocus. The local heating fashions the defocusing and the downwind advection of the warmer air causing the laser beam to deflect and lose focus towards the downwind

direction (Sprangle et al. 2007). Hence, thermal blooming is related to the atmospheric absorption of laser beam energy and the subsequent heating of the atmospheric medium - which in turn affects the laser beam propagation. This phenomenon is unique to high energy laser because of the intense energy source for gaseous and aerosol absorption. The effects on laser beams are even more prominent in the presence of a stagnation zone, defined as regions where the flow velocity is zero (Sprangle et al. 2007).

B. VARIABLES TO DESCRIBE SCINTILLATION

The Structure-Function Parameters

The most critical parameter providing information about atmospheric scintillation is C_n^2 (Wyngaard et al. 1971). Tatarskii's (1971) definition of C_n^2 is related to the structure-function of the refractive index defined in Equation (1). This refractive index expression also gives "the most theoretical analyses of the scattering of electromagnetic and optical radiation by turbulence" (Wesely 1976).

$$\overline{[n(x,t) - n(x+r,t)]^2} \equiv \overline{(n-n')^2} \tag{1}$$

Here, the overbar denotes the ensemble average; where n is the changing refractive index at point x and n' and at point $x+r$ (Wyngaard and Kosovic 1994). In Equation (2) n is defined as where v is the phase speed, and $\boldsymbol{c}$ is the speed of light in a vacuum.

$$n = \frac{c}{v} \tag{2}$$

In the inertial subrange of turbulence, turbulence is assumed to be isotropic and hence dependent only on r, the structure function can then be expressed in terms of the refractive index structure parameter, C_n^2, as defined in Equation 3:

$$\overline{(n-n')^2} = C_n^2 r^{2/3} \tag{3}$$

Wyngaard (1978) explicitly express the refractive index for electromagnetic radiation n terms of temperature and humdity (Equation(4)) so that C_n^2 may be expressed regarding the structure-function parameters for temperature and water vapor pressure (Wyngaard and Kosovic 1994).

$$n = aT + be \tag{4}$$

where T is temperature and e the water vapor pressure. The coefficients a and b are dependent on wavelength. The structure parameter C_n^2 can then be expressed more explicitly in terms of each structure function parameter: C_T^2 for temperature, C_{eT} for cross-correlation contribution of temperature and water vapor pressure, and C_e^2 for water vapor pressure (Wyngaard and Kosovic 1994) as shown in Equation (5).

$$C_n^2 = B_1 C_T^2 + B_2 C_{eT} + B_3 C_e^2 \tag{5}$$

Here B_1, B_2, and B_3 represent the calculated constants to radiational wavelength dependent coefficients. Equation (5) will be used in this research to calculate C_n^2 based on a high-rate sampling of temperature and water vapor pressure. The magnitudes and relative importance of B_1, B_2, and B_3 will be evaluated.

The Rytov variance is another parameter that can be used to represent the effect of scintillation (Sprangle et al. 2007). It is calculated at different turbulence mediums and for different wavelengths (Thomas 2005). As the index of scintillation increases, the Rytov variance value also increases.

The Fried Parameter is an alternative measure of scintillation which emphases the diameter of an aperture lens size, for which the phase variance is approximately one. Fried parameters are used to quantify the combined strength of the turbulence. It is given by Equation (6) and is dependent on turbulence profile of C_n^2, the zenith angle (ς), and the wavelength (k) (Hardy 1998).

$$r_0 \equiv (0.423k^2 \sec\varsigma \int_0^\infty C_n^2(z)\, dz)^{-3/5} \tag{6}$$

C. SCINTILLATION (C_N^2) MODELS

Various C_n^2 models exist at many levels of complexity. In this section, we briefly introduce a few most commonly referenced models to include NSLOT, NAVSLaM, PAMELA, and the Hufnagel-Valley models.

1. NSLOT

The Navy Surface Layer Optical Turbulence (NSLOT) model provides a method to estimate C_n^2 from routine meteorological observations. NSLOT was developed for application in the marine environment. The C_n^2 is diagnosed based on the Monin-Obukhov Similarity Theory (MOST) using input of mean wind, temperature, humidity, and sea surface temperature. According to Doss-Hammel (2004), "specific parameter values such as surface roughness has been "hard-wired" into the model." NSLOT performs well for common open-ocean conditions (Doss-Hammel 2004). Currently, NSLOT has been incorporated into NAVSLaM to be discussed next.

2. NAVSLaM

The Navy Atmospheric Vertical Model (NAVSLaM) is a 1-dimensional diagnostic model based on measured or modeled near-surface mean quantities. "NAVSLaM employs MOST to describe the air-sea fluxes and the near-surface profiles of temperature and humidity" (Frederickson 2015). It was originally developed to quantify EM refractivity near the surface as a result of evaporation ducts. NAVSLaM was recently modified to include calculations of C_n^2 for optical turbulence application in the marine atmospheric surface layer using the basic formulations employed in NSLOT.

3. Hufnagel-Valley Model

The Hufnagel-Valley model is an empirical simple C_n^2 model used for altitude scaling. This model was developed by R.E. Hufnagel (1974) and was amplified with a boundary layer term spreading the model to the surface, as proposed by G.C. Valley (1980) (Lawson and Carrano 2006). This model was empirically fitted to the dependency observations of C_n^2 in a mid-latitude climate. The altitude dependent C_n^2 is given in Equation 7, where A represents the C_n^2 near the surface and v represents the wind speed at a high altitude:

$$C_n^2(h) = 5.94 \times 10^{-53} (v/27)^2 \, h^{10} e^{(-h/1000)} + 2.7 \times 10^{-16} e^{(-h/1500)} + A e^{(-h/100)} \quad (7)$$

The Hufnagel-Valley model has been widely used in the HEL community mainly because of its simplicity and its capability to extend to the upper boundary layer. However,

careful evaluation of an empirical model like this should be done to ensure its broad applications.

4. PAMELA Model

The PAMELA model is another scintillation model. PAMELA is a reasonably straightforward over land model to implement, but due to the model's high sensitivity towards low wind speeds -and having a lack of a surface characterization, a successful prediction for maritime conditions cannot be attained (Doss-Hammel et al. 2004).

5. HELCAP

Throughout the Department of Defense, the modeling and characterization of atmospheric effects on the propagation of HEL beams are of critical importance. The development of the High Energy Laser Code for Atmospheric Propagation (HELCAP) code, created by the U.S. Naval Research Lab, is a unique simulation capability that models a wide parameter space of laser propagation (Zohuri 2016). The HELCAP code has allowed scientists to quantify the power of HEL weapons megawatts class by evaluating the effects of stagnation zone in a maritime atmosphere (Sprangle et al. 2007). The HELCAP code provides a unique capability to study the complex physics of HEL weapons engineering and aid in future laser development.

6. Wave-Train

Wave-Train is a software tool for the reliable modeling of advanced optical systems (Coy 1999). It provides a MATLAB interface for post-processing data from laser weapons systems and compensated imaging systems. "Wave-Train uses a modeling approach known as 'wave optics,' in which optical wavefronts are modeled using two-dimensional meshes of complex numbers" (Coy 1999). Wave optics is used for predicting the performance of optical systems in a strong turbulent atmosphere.

7. Wave-Prop

Wave-Prop is another wave optics simulation system that uses MATLAB. Wave-Prop is a tool that assists in basic propagation research as well as evaluation of optical system performance. Developed by the Optical Sciences Company, it can be used to gain quick insight into propagation problems or to model highly detailed systems and applications including laser weapons, laser communications, and imaging (Optical Sciences Company 2011).

D. OPTICAL SYSTEMS—SENSORS AND HEL WEAPONS USAGE

Various optical sensors are used in detecting and identifying targets. Choices require the consideration of the vagaries in transmitting and scattering in the atmosphere which requires shortwave propagation to scan images at a blurring distance (Koretsky 2013). Optical Targeting Lasers (OTL), for instance, help shooters to focus and adjust accuracy while aiming. OTLs improve basics such as “aiming” and “triggering.” Lasers are specially made to fit in firearms and are made easy to install and use. For HEL weapons, absorption of shortwave radiation causes an increase in the thermal blooming through heated aerosols (Sprangle et al. 2007). The effect of shortwave propagation on sensors enables it to detect targets that are dim and obtains targets from complex backgrounds (Koretsky 2013). Under good conditions, HEL weapons can propagate long distances (Sprangle et al. 2007).

One of the most significant problems facing optical lasers is decreased performance in the polluted air. By using laser technology, we can study, observe and monitor the earth’s atmosphere to mitigate this issue. The growth and development of industries and urbanization have caused and abundance of atmospheric pollution. Therefore, research has applied the development of prototypes using the Laser Heterodyne Radiometer (LHR) to offer a good spatial resolution (Weidmann et al. 2007). Viewing the atmosphere from space gives a global view of the atmospheric composition and processes.

THIS PAGE INTENTIONALLY LEFT BLANK

III. DATA COLLECTION AND METHODOLOGY

A. CASPER-EAST FIELD CAMPAIGN

CASPER is a Multidisciplinary University Research Initiative (MURI) funded by the U.S. Office of Naval Research (ONR). CASPER is comprised of two major field campaigns proceeded by a pilot experiment in Monterey Bay from April 20 to May 5, 2015. The CASPER-East field campaign occurred off the coast of Duck, North Carolina during October/November 2015 time frame. Figure 5 shows the shore site of CASPER-East located on the complex of the Field Research Facility (FRF) of the U.S. Army Corps of Engineers with a 500 m long pier into the water. CASPER-West field campaign was conducted offshore of Point Mugu, California in September and October of 2017. This project uses data collected in CASPER-East field campaign. The focus of CASPER-East is to assess the uncertainties in evaporation duct modeling and the effects of a heterogeneous marine environment on EM/EO propagation (Wang 2017).

Figure 5. U.S. Army Corps of Engineers Field Research Facility Pier, Duck, North Carolina. Source: Field Research Facility (1992).

The measurements include multiple research sites and platforms as shown in Figure 6. Measurements of CASPER-East were coordinated among major platforms including two research vessels, a research aircraft, and the shore site based at the Duck Pier. The coordinated measurement segments obtained range-dependent propagation loss accompanied by concurrent environmental refractive conditions along propagation paths. This thesis research uses the measurements from the research aircraft described in the following sections.

Figure 6. Data Collection Platforms Used for CASPER East Field Campaign. Source: Wang (2017).

B. AIRCRAFT MEASUREMENTS FROM CASPER-EAST

All data used in this study was collected from the research aircraft during CASPER-East Field campaign: the Center for Interdisciplinary Remote Piloted Aircraft Study Twin Otter and the Controlled Towed Vehicle tethered to the Twin Otter. The Twin Otter with the CTV deployed below is shown in Figure 7. The fast-moving platform is capable of sampling over larger areas so that spatial variability can be examined in a short time-period (Kalogiros and Wang 2011). In the case of CASPER-East, the aircraft aptly complements measurements from the slow-moving ships and fixed location measurements from buoys, pier, and land towers. The extensive area coverage provided a sampling of wind, wave and SST heterogeneity and ducting conditions of the measurement region. Figures 10 and 11 show the area coverage from all CASPER-East flights and a schematic of the planned three-dimensional flight path. There was a total of 10 flights during the CASPER-East field campaign.

Figure 7. CIRPAS Twin Otter Towing Controlled Towed Vehicle below for Data Collection. Source: Khelif (2013).

1. CIRPAS Twin Otter

The CIRPAS Twin Otter (TO) is an instrumented twin-engine turboprop aircraft. In this research Twin Otter flights provided "measurements of mean & fluctuating *u*, *v*, *w*, mean & fluctuating *T*, *e*, *p*, sea surface and "sky" IR temperatures" (Wang 2017), and platform motion. Further data processing resulted in motion-corrected turbulence and calculated turbulent fluxes. Figure 8 details the instrumentation on CIRPAS Twin Otter aircraft, the red circle highlight the 5-port Radome Wind System used for measuring air velocities relative to the aircraft.

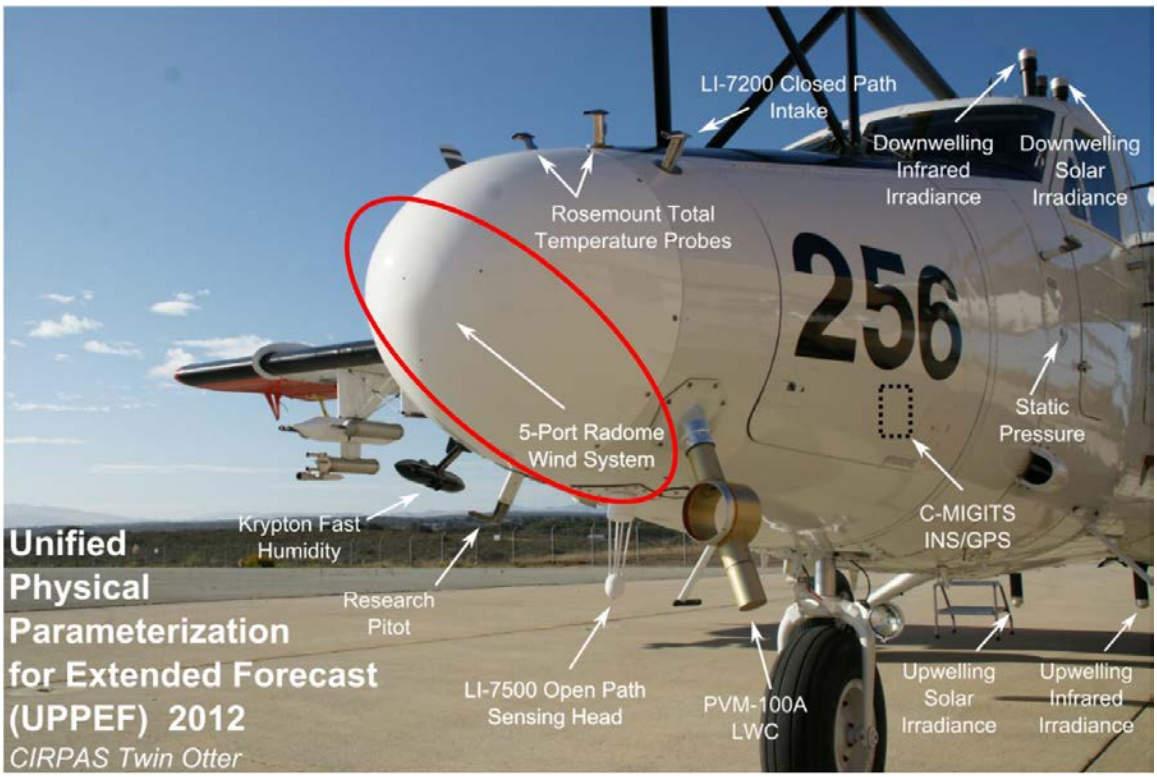

Same instrument setup was used in CASPER-East.

Figure 8. CIRPAS Twin Otter Instrumentation Setup Used for the Unified Physical Parameterization for Extended Forecast. Adapted from Khelif (2013).

2. Controlled Towed Vehicle

The Controlled Towed Vehicle (CTV) is a modified target drone instrumented for boundary layer measurements much the same way as that on the radome of the Twin Otter. Figure 9 shows multiple view angles of the CTV instrumentation. Khelif (2017) suggest "the CTV is capable of active altitude control via controllable wing, and it can maintain radar altitude as low as ~9 m above ocean surface while being towed from the Twin Otter at ~300 m above." Given that the Twin Otter has a minimum altitude of ~30 m, the main advantage of the CTV is the direct measurement of mean and fluctuations of meteorological parameters and fluxes at the canonical ~10 m height above the air-sea interface. While air-sea flux divergence is traditionally thought to be negligible between 30 m and 10 m and can be approximately corrected, CTV removes the necessity for such

corrections and underlying assumptions (Kalogiros and Wang 2011). Moreover, the mean wind is directly measured at ~10 m without invoking MOST.

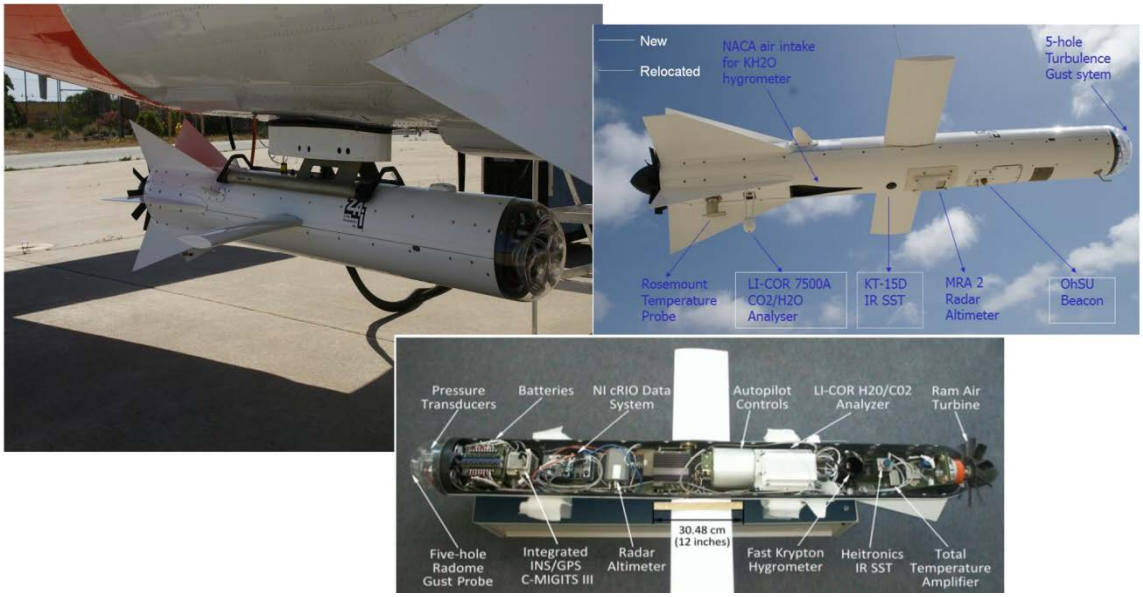

Figure 9. CIRPAS Controlled Towed Vehicle Mounted to the Twin Otter before Deployment (top left), Instrument Locations Seen from Outside (top right) and Inside (lower panel). Adapted from Khelif (2016).

With similar instrumentation, the Twin Otter and the CTV make simultaneous measurements at two levels when CTV is deployed. In case of a shallow boundary layer, the use of CTV becomes crucial, as runs at several levels within the surface layer will be flown to determine the mean gradients, flux divergence, and deviation from MOST profiles.

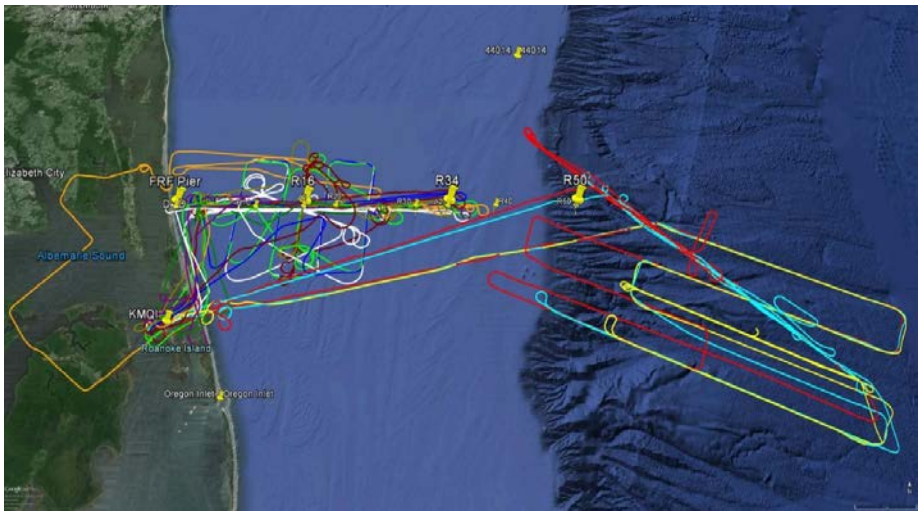

Figure 10. Flight Tracks of all Twin Otter Flights during CASPER-East. Adapted from Khelif (2016).

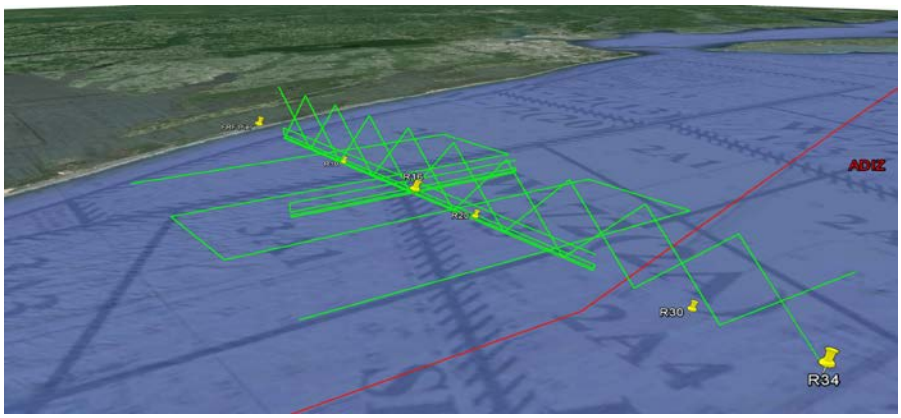

Figure 11. A Three-Dimensional View of an Example Flight Path of TO/CTV during CASPER-East. Source: Khelif (2016).

C. CASPER-EAST CTV DATA PROCESSING

The CTV data from CASPER-East was initially post-processed and quality controlled by Dr. Djamal Khelif, one of the CASPER collaborative principal Investigators from University of California, Irvine. The major part of this post-processing includes turbulence retrieval to remove platform motion from the radome measurements. In addition, the CTV measured SST was corrected for infrared reflection from the sky. The processed 40-Hz data was made available to CASPER collaborators.

THIS PAGE INTENTIONALLY LEFT BLANK

IV. DATA ANALYSES AND RESULTS

Analyses and results are shown and discussed in this chapter with a focus on the variability of C_n^2 in marine environments.

In the past, oceanic measurements of C_n^2 used manned aircraft, which could not fly below the 30 m flight level. The development and use of the CTV allowed for similar measurements to be taken at the 10 m flight level. The objective of this study is to evaluate the use of this aircraft based measurements over the ocean to examine physical processes contributing to optical turbulence. MATLAB was used as an analysis tool for this thesis work to calculate various quantities and produce final figures.

A. SELECTION OF DATA SECTIONS

The first step in data analyses was to identify sections of data with optimal measurements. Figure 12 depicts the process of data selection using an example from 14 October 2015. We examined the temporal variation of the CTV altitude, heading, and longitude during one flight to select sections of data from approximately the same altitude and when the aircraft was flying at a constant heading. Each selected data section was referred to as one sampling "leg."

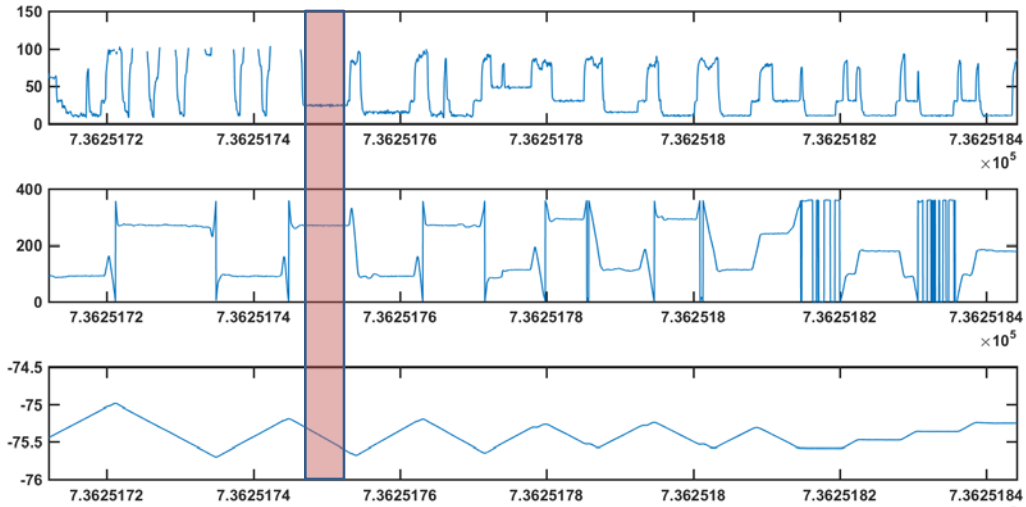

Measured CTV altitude (top), heading (middle), and longitude (bottom) used to define sampling 'legs' for quantitative analyses. The segment highlighted in orange shows an example of the selected leg with constant altitude and heading.

Figure 12. An Example of Selection of Useful Data Sections

Figure 13 depicts all selected leg sections from the flight shown in Figure 12 in varying colors. During this flight, 16 leveled legs were selected ranging from 9 m to about 50 m above the surface. Leveled legs shorter than 1 km were ignored as they do not provide sufficient data amount to yield results that are statistically significant. Figure 13a shows the altitude variation while Figure 13b displays flight track on the horizontal plane. Most of the straight leg measurements were made in the east-west direction and in the north-south direction, which is the case for most of the CASPER-East flights over the continental shelf. Over the Gulf Stream (GS) region, flight legs were generally in the direction crossing the SST front.

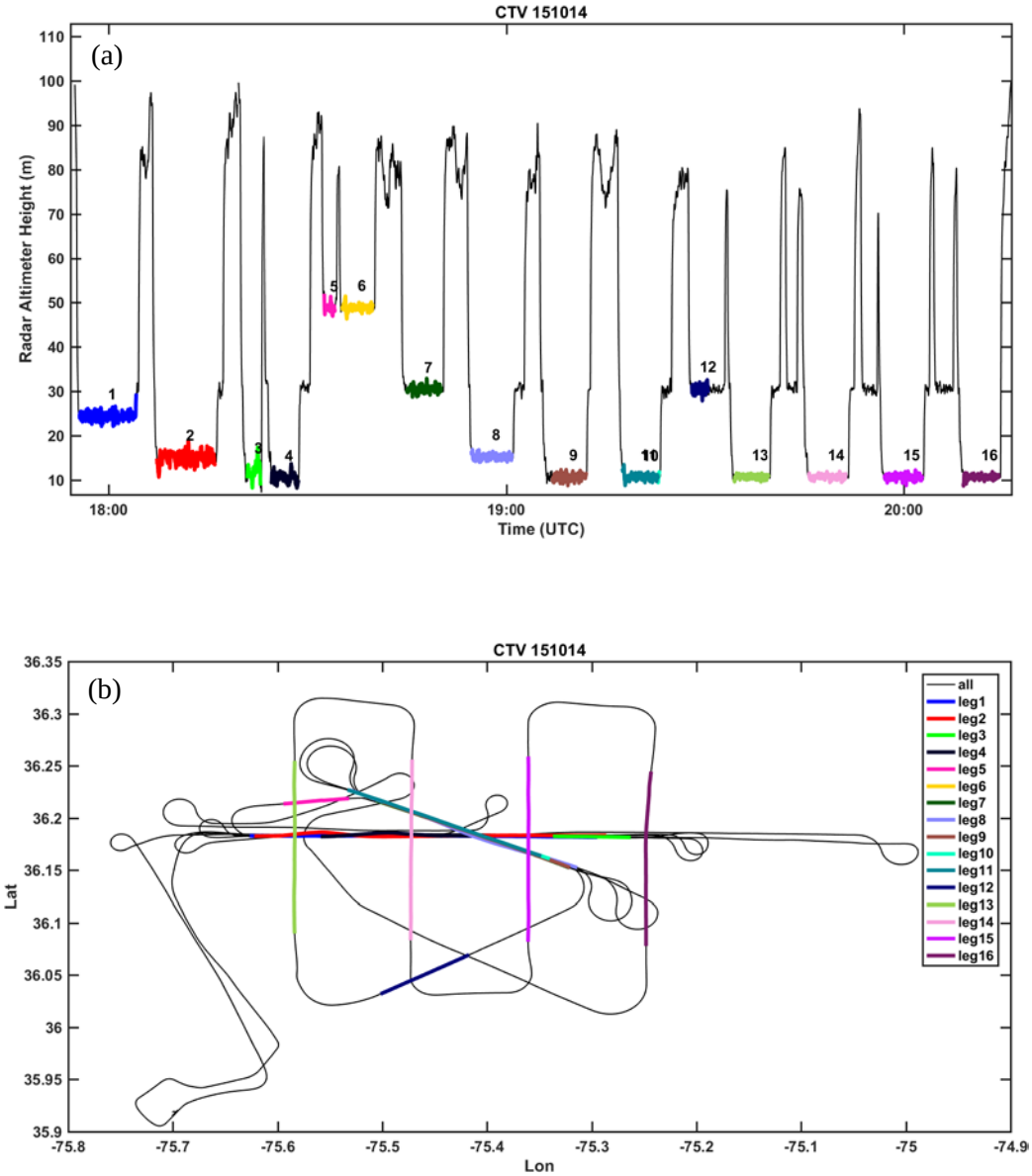

(a) CTV altitude variation vs. time during the flight on 14 October, 2015. Analyses of vertical variations were made using two groups of legs (legs 1–4 and 6–9) where measurements within each group were taken in proximity to time. (b) A horizontal view of the flight track for the entire flight and selected data sections.

Figure 13. Illustrations of the Data Sections Chosen for Analyses to Reveal Vertical and Horizontal Variabilities

Leg selection was performed for all ten flights during the CASPER-East field campaign. For this study, a total of 130 data legs were selected and analyzed. Table 1 summarizes all the resultant legs from all flights based on the flight date. The groups of legs used for vertical variability study are listed in the column titled “Legs for Altitude Variability.” In the column titled “Legs for Spatial Variability,” each group represents measurements from the same level at different locations (legs 13–16 for example in Figure 13b) or repeating along the same line (legs 10–11 in Figure 13b). The rest of the identified legs are grouped into the ‘Others’ column.

Table 1. Summary of CASPER-East Flight and Selected Data Legs for Different Types of Analyses

Date (mm/dd/yy)	Flight Duration (hr)	Number of Usable Legs (#)	Legs for Altitude Variability (leg #)	Legs for Spatial Variability (leg #)	Others (leg #)
15/10/14	4:00	16	1-4, 6–9	10-11, 13–16	5, 12
15/10/16	5:00	14	1-5, 6–7, 8–9	11-14	10
15/10/17	4:30	18	4-5, 10–13	2-3, 7–9, 15–18	1, 6, 14
15/10/18	5:15	16	1-4, 8–9, 9–10, 14–16	5-7, 11–13	
15/10/21	5:30	11	4-5, 9–11	2-3, 7–8	1, 6
15/10/27	1:15	5	3-5	1-3	
15/10/30	3:15	13	2-4, 12–13	5-8, 9–10, 11–12,	1
15/10/31	5:15	15	1-3, 12–15	4-5, 6–7, 9–10, 11–12	8
15/11/01	5:15	14	1-2, 13–14	4-5, 7–9, 10–11	3, 6, 12
15/11/03	2:15	8	2-3, 5–8	1-2	4

For each of the selected legs, 40-Hz sampled data of temperature, water vapor, turbulence wind components (*u*, *v*, and *w*) were used to calculate all turbulence statistics including mean wind, temperature, and specific humidity and fluxes of momentum, sensible (SHF), and latent heat (LHF). The same data was also used for making spectra analyses and obtaining the structure parameter of refractivity (C_n^2), temperature (C_T^2), water vapor (C_e^2), and the cross-correlation between temperature and water vapor (C_{eT}), the terms defined in Equation (5). The 1-Hz calibrated SST, and the mean temperature was used to derive the air-sea temperature difference (*ASTD*). These constitute the results to be discussed in the following sections, in which we will discuss the horizontal and vertical variabilities as well as the effects of wind speed and *ASTD* on parameters related to optical turbulence.

B. HORIZONTAL VARIATIONS

The horizontal variations are shown with several examples from different flights. The first example given in Figure 14 was measured on a day with moderate northerly wind over the shelf region. The surface layer in the case was very convective (unstable) with *ASTD* in the range of 2–3°C. As a result, we obtained positive SHF peaking up to 20 Wm^{-2} with corresponding LHF values around 100 Wm^{-2} in the nearshore region, especially in the first 20 to 23 km of the leg. I observed a gradual increase in *ASTD* at this part of the leg, showing the boundary layer becoming progressively unstable toward offshore. There is also a slight increase in wind speeds from 3 to 5.5 ms^{-1} in this section of data. The corresponding increase in all three fluxes is observed in the same region of progressively increasing *ASTD* and mean wind. (Figure 14a).

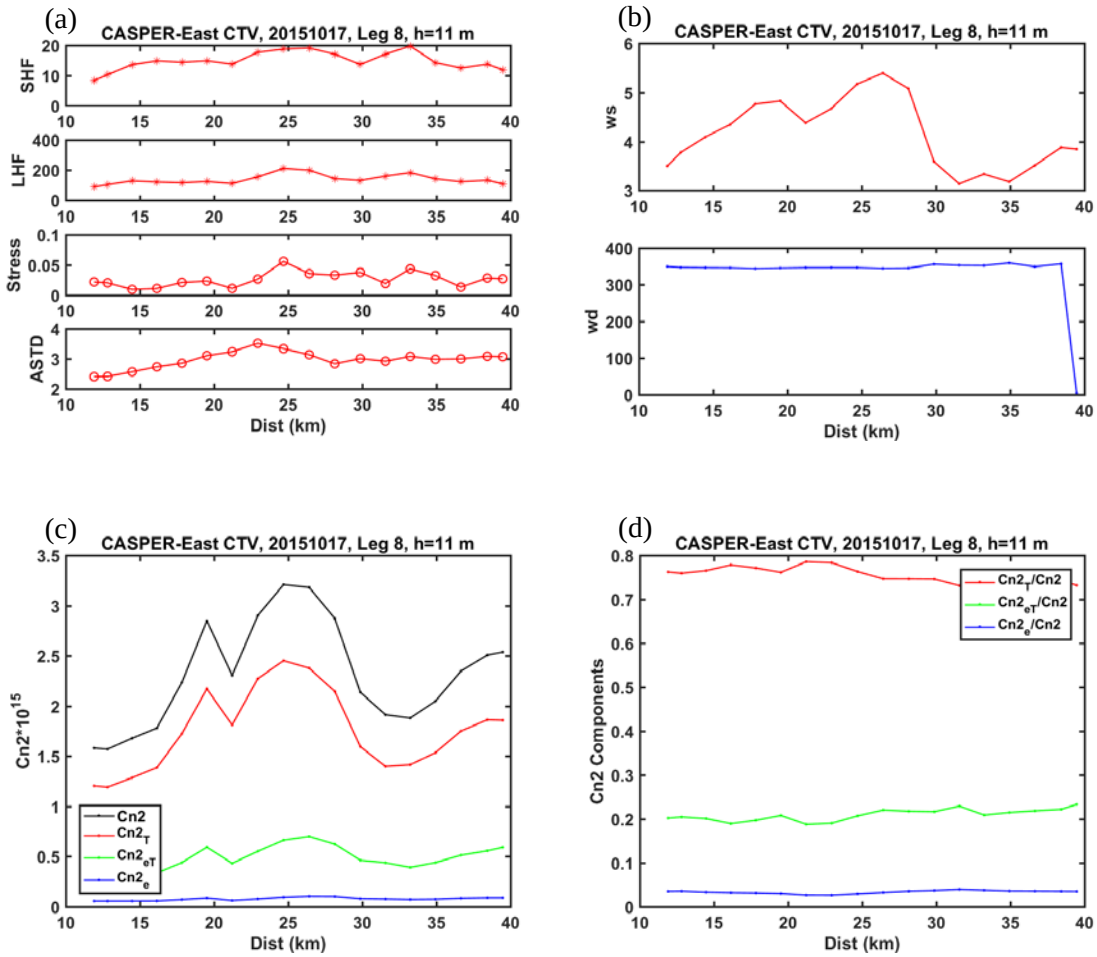

(a) Turbulent fluxes to include sensible heat flux (SHF, Wm^{-2}), latent heat flux (LHF, Wm^{-2}), and momentum flux (Stress, Nm^{-2}). The air-sea temperature difference (*ASTD*, Kelvin) is the bottom panel; (b) wind speed (ms^{-1}) and direction; (c) calculated C_n^2, C_T^2, C_e^2, and C_{eT} multiplied by 10^{15}; (d) Percentage contribution of each component of C_n^2 to quantify individual contributions.

Figure 14. Horizontal Variations of Boundary Layer Mean, Turbulence, and Optical Turbulence Properties Calculated Based on Measurements from Leg 8 at 11 m above Sea Level on 17 October 2015

The variations in *ASTD* and the mean wind speed appear to contribute to the variations of optical turbulence properties as well (Figure 14c). Figure 14c shows an increase in all components of the C_n^2, except C_e^2, in the initial 23 km of the leg. I also observed the dominant contribution of C_T^2 to total C_n^2 where C_T^2 composed 78% of the total C_n^2, and the cross-correlation between temperature and water vapor pressure, in this case, contributes to around 20% of the C_n^2. The contribution from the C_e^2 is meager, less than 5%.

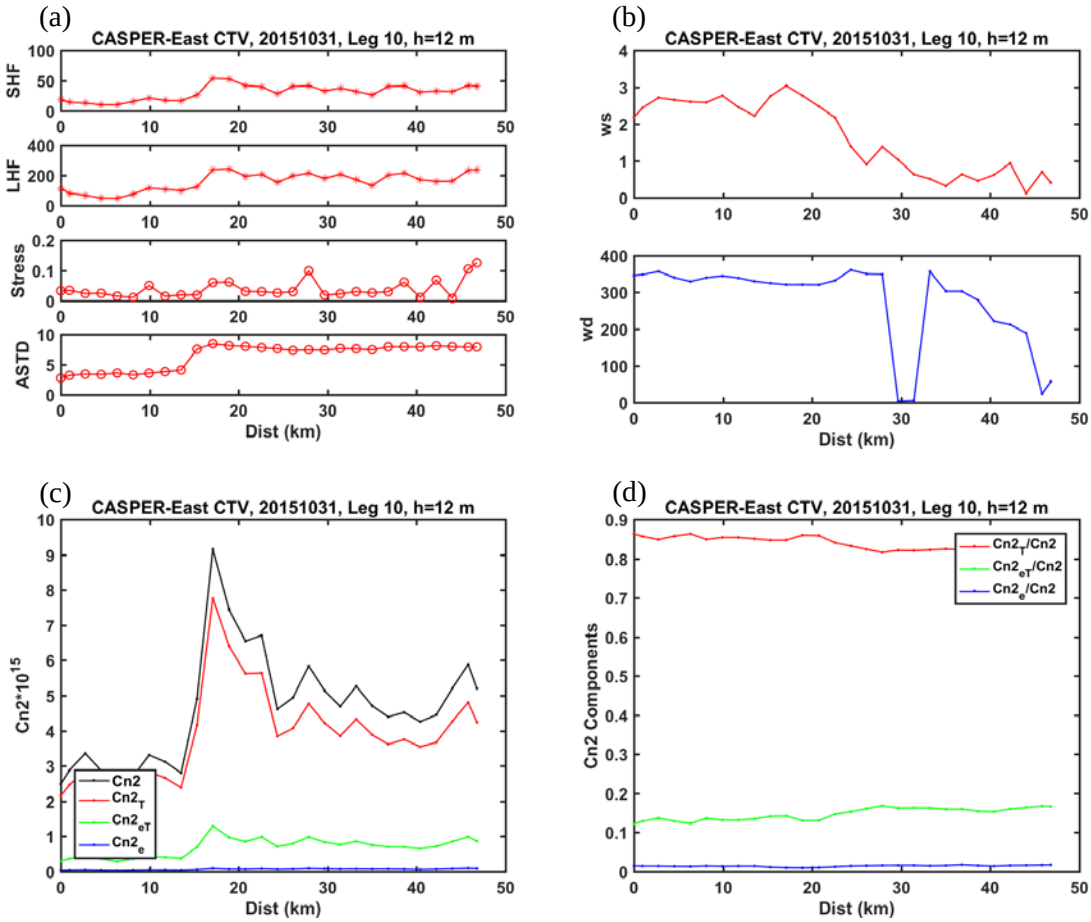

Measurements were made over the Gulf Stream.

Figure 15. Same as Figure 14, Except for Leg 10 at 12 m above Sea Level on 31 October 2015

Another example of horizontal variability is shown in Figure 15, except this example was taken from a flight over the Gulf Stream. In this case, an SST front was identified at ~15 km distance from the beginning of the leg. The SST front was noticeable in *ASTD* (Figure 15a) as well, where the magnitude of *ASTD* increased from 4 to 9 K.

Unlike over the shelf region, the boundary layer on each side of the GS front appears to be rather homogenous with small *ASTD* variations. The weak wind was generally from the north in the range of 0.5 ms^{-1} to 3 ms^{-1}. Turbulent fluxes show significant variation in response to the SST front. Over the cold-water region, we see SHF in the range of 12 Wm^{-2}, and over the warm water region, we see values increase by

five times to ~50 Wm^{-2}. Significant variation was seen with the LHF as well, changing from ~100 Wm^{-2} to ~250 Wm^{-2}. The momentum flux was relatively weak, which is consistent with the weak wind in this case. Figure 15c also depicts the significant variation across the SST front from all components of C_n^2. Over the cold-water region, C_n^2 values were between ~2×10^{-15} and ~4×10^{-15}. Over the warm water region magnitudes of C_n^2 were between ~5×10^{-15} and ~9×10^{-15}, twice as large compared to the relatively cold-water region.

Although both regions are still in the unstable thermal stability regime because of the positive *ASTD*s, there are slight variations in the component contributions on the two sides of the Gulf Stream. Over the cold-water region, the C_T^2 composed about 88% of the total C_n^2, over the warm-water region, this value drops to about 85%. The opposite trend is seen in the contribution from the cross-correlation component where C_{eT} contributed 12% on the cold-water side, and around 15% on the warm-water side. Moreover, there appear to be some slight changes in the C_e^2 as well, although the overall magnitude is much smaller, insignificant compared to the other two components.

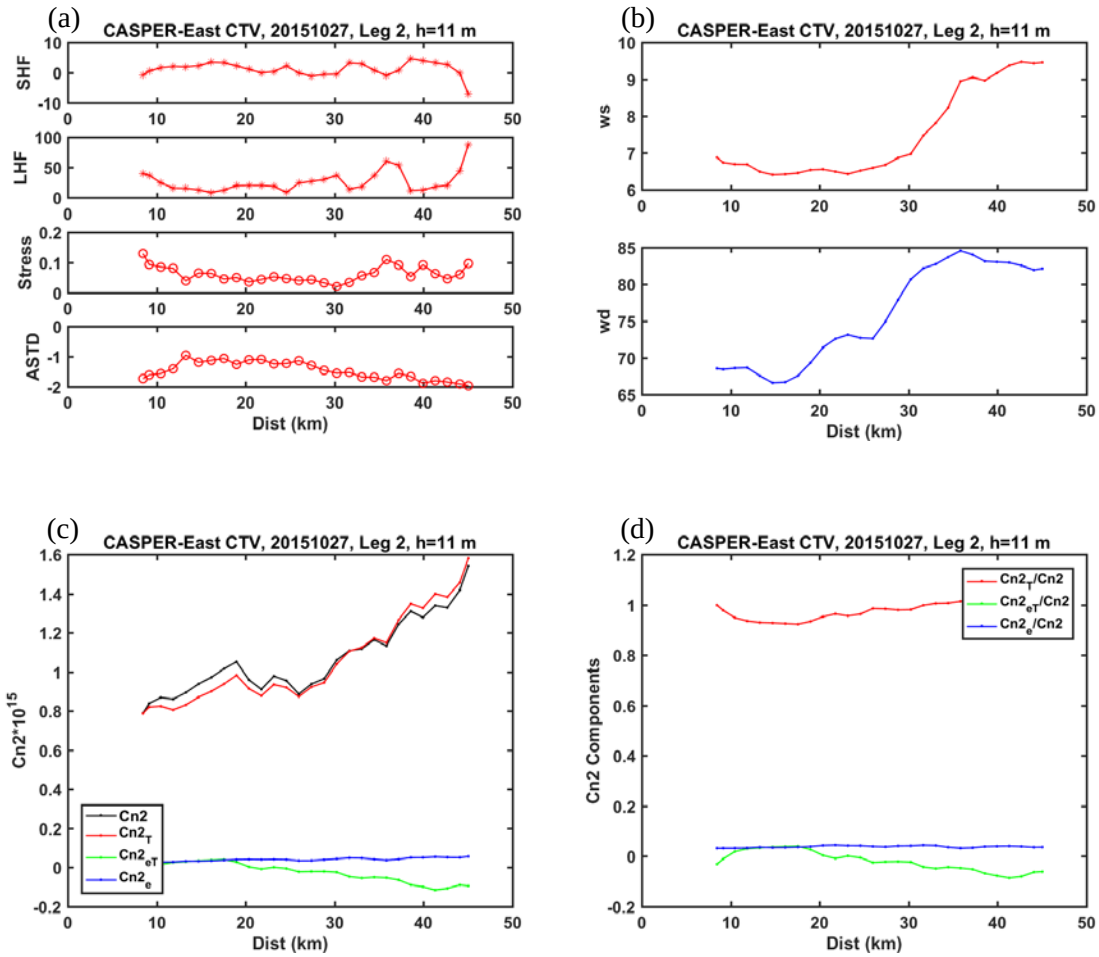

Measurements were made over the stable environment.

Figure 16. Same as Figure 14, Except for Leg 2 at 11 m above Sea Level on 27 October 2015

Figure 16 shows an example of varying thermal stability on all components of C_n^2. In this case, *ASTD* is persistently negative indicating stable thermal stratification of the surface layer. The wind speed, in this case, is higher compared to the previous cases ranging from ~6 ms^{-1} to ~9 ms^{-1} with some slow variation from the northeast wind direction.

Near-zero sensible heat flux was observed from most of this measurement leg, particularly in the low wind section. When wind speed increased after the 40 km into the leg, the larger magnitude of SHF and LHF were observed corresponding to the increased wind speed.

From Figure 16c we observe a consistent trend between C_n^2 and C_T^2 starting from ~28 km distance corresponding to the observed increase of wind speed. Apparently, in this case, wind speed is a major factor affecting the variation of C_n^2. Interestingly, the cross-correlation of temperature and water vapor are very small or negative. In the initial 20 km of the leg, the *ASTD* is relatively small, and that corresponds to near zero C_{eT}. Beyond 20 km distance, the gradual increase in the magnitude of C_{eT} seems to correspond with the changes in the magnitude of the negative *ASTD* (stable boundary layer).

A different fractional contribution of the components is seen in Figure 16d because of the negative C_{eT} contribution. The C_T^2/C_n^2 is close to 100%, C_e^2/C_n^2 is still very small, in the range of 3%, and the negative contribution from C_{eT} is in the range of -5%. The negative value of C_{eT} corresponds to the more substantial magnitude of negative *ASTD*.

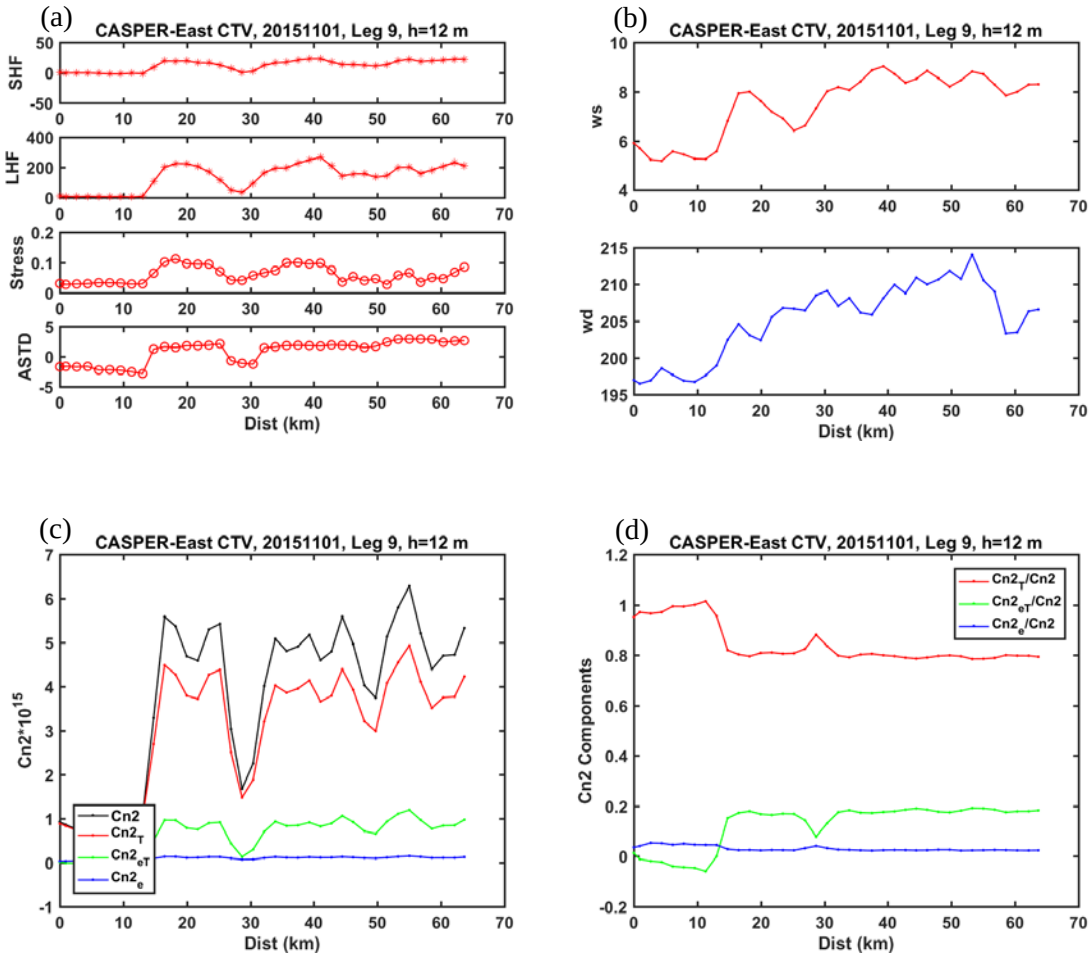

Measurements were made over a stable to unstable environment over the Gulf Stream.

Figure 17. Same as Figure 14, Except for Leg 9 at 12 m above Sea Level on 01 November 2015

Another example of the thermo-stability effects is shown in Figure 17 taken from a low-level leg of 12 m in altitude. In this case, thermal stratification changes across the SST front. Unstable conditions were measured over the warm-water region and stable condition over the cold-water region. I noticed a patch of cold water within the warm section with nearly neutral or slightly stable thermal stratification. Weaker wind speed is seen in the cold stable stratification region, and a slight increase is observed over the warm region.

The turbulent fluxes correspond to *ASTD* and the wind speed variation very well. Over the cold region, SHF is slightly negative near zero. Over the warm region, SHF is

~25 Wm^{-2} with a minor dip in the slightly stable section around 28 km distance. This is likely a cold filament of water observed within the Gulf Stream. This slightly stable region is seen consistently in Figure 17a across all variables. The warm and cold regions on two sides of the Gulf Stream are vastly different in SHF: 10 Wm^{-2} on the cold side and increases to 200 Wm^{-2} on the warm side, suggesting the impact of thermal stability. In this case, we also observe a significant change in surface stress with the marked increase over the warm water region. The change in momentum flux should be a result of both thermal stratification and the increased wind speed over the warm-water section.

In the subplot for C_n^2 (Figure 17c) the variations of C_n^2 with thermo-stability can be identified over the cold-water region and over the cold filament. Stable stratification results in much lower C_n^2 and all its components. A significant sudden change in C_n^2 is seen over the SST front. We observe C_n^2 changing from 1×10^{-15} to 5 times larger over the warm water section. This variation is shown in the component contribution plot in Figure 17d, where we can see the C_{eT} contribution changing from negative to positive across the SST front. Results from this example are consistent with our analyses of previous examples that stable stratification results in a negative C_{eT}. The C_T^2 contribution changes across the SST front as well. In the stable condition, as what we observed in the previous examples, we see around 98% contribution from C_T^2. In the unstable condition, however, this contribution becomes ~80%, consistent with previous results in the unstable condition (e.g., Figure 16).

C. VERTICAL VARIATIONS

CTV measurements were made at multiple levels in the lower boundary layer. These sampling in vertical stacks were designed to be completed in a short time-period, about one hour so that they can be used to indicate the vertical variation of the boundary layer properties with minimum contamination from temporal variabilities. In this section, the vertical variations of optical turbulence are shown using these groups of vertical stack measurements. All groups of legs are also indicated in Table 1.

The first example of the vertical variation is shown in Figure 18 taken the shelf region in weak winds. The temperature profile shows rather weak, close to neutral

thermo-stability. Water vapor specific humidity, on the other hand, shows a clear negative gradient in the lowest 50 m of the boundary layer. From the lowest level of these legs, we observed an *ASTD* of 1.3 K representing a weakly unstable stratification. In this case, we can see the lowest measurement leg at 11 m above sea level (ASL) showing a C_n^2 of 0.8×10^{-15}. A few meters above at 15 m, C_n^2 sharply decreases to 0.4×10^{-15} (Figure 18b). Figure 18c shows the vertical variation of the component contribution to C_n^2. I found that the component contributions do not vary significantly with height: ~80% from C_T^2, ~17% from C_{eT}, and only ~5% in C_e^2.

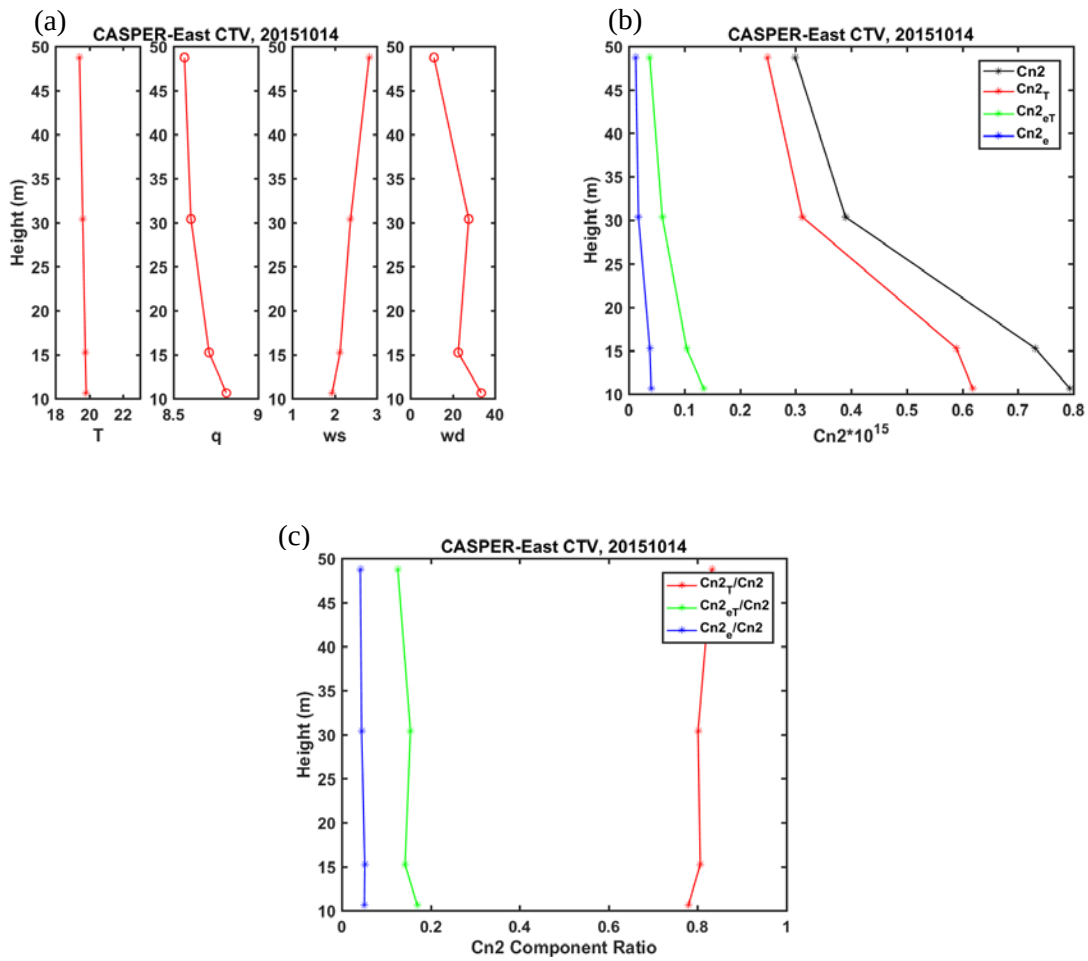

The measurements were made in weak, unstable conditions over the shelf region.

Vertical variations of (a) mean temperature (T, ^{o}C), specific humidity (q, g Kg^{-1}), wind speed (ws, ms^{-1}), and wind direction (wd, deg); (b) C_n^2 and its components; and (c) ratio of C_T^2, C_e^2, and C_{eT} to C_n^2.

Figure 18. Vertical Variations of Mean and Optical Turbulence Properties Observed from Legs 6–11 on 14 October 2015

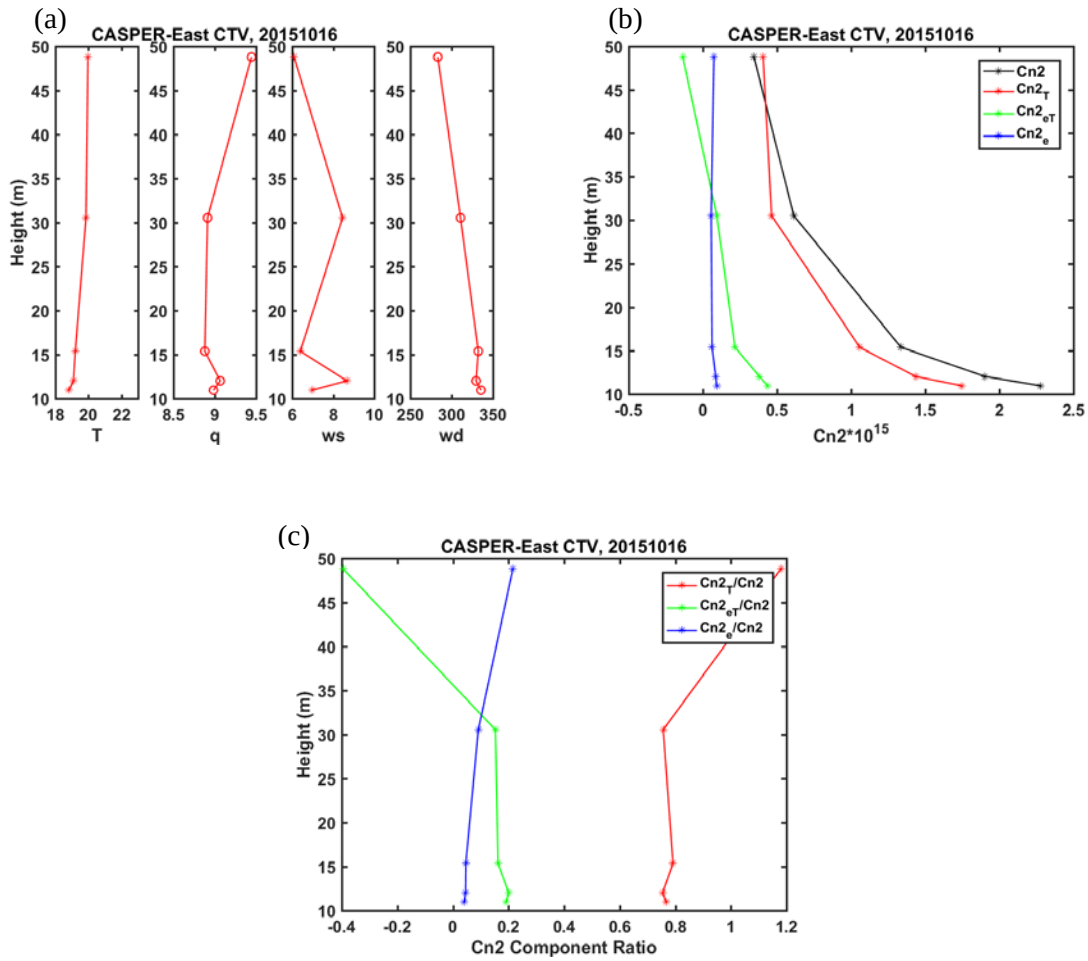

Figure 19. Same as Figure 18, Except for Legs 1–5 on 16 October 2015, over the Shelf Region

Another example over the shelf region is seen in Figure 19. It shows a moderate wind condition with a rather weak but stable temperature profile. In this case, we observed an *ASTD* of 1.8 K in the lowest level indicating an unstable surface layer in the lowest 11 m. The surface layer, in this case, is quite complicated. The total measured C_n^2 is of 2.3×10^{-15} which decreases to below 0.5×10^{-15} 30 m above the surface. In this case, the sign of C_{eT} is consistent with an unstable surface layer in the lowest three levels, and the negative value at ~50 m shows the effect of stable stratification seen before. C_T^2 composed of ~78%, the cross-correlation component C_{eT} 20% in the unstable levels with a negative contribution to C_n^2 only at the highest level (~50 m ASL). C_e^2 still is very small, in the range of 2%, at all levels.

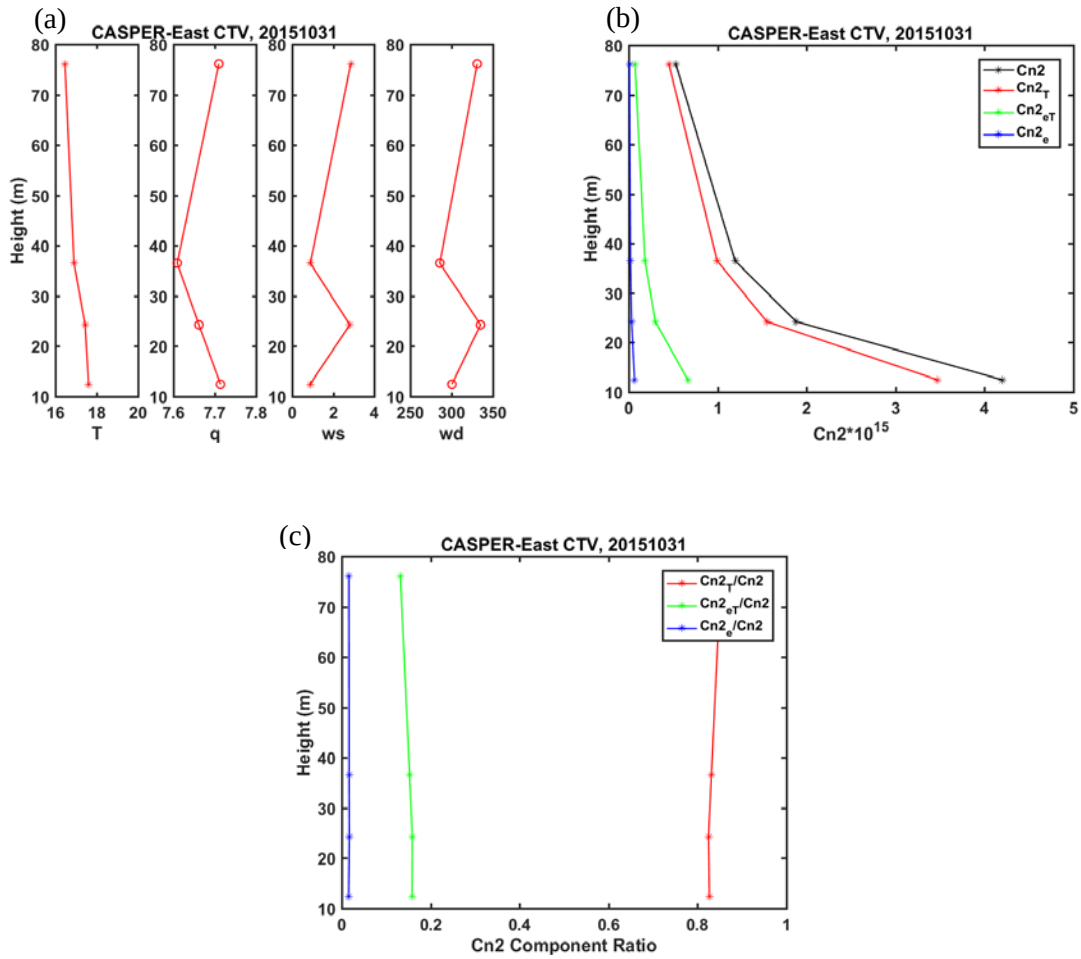

Figure 20. Same as Figure 18, Except for Legs 12–15 on 31 October 2015, over the Gulf Stream

A vertical profile from over the Gulf Stream is depicted in Figure 20. In this case, mean *ASTD* at the lowest leg was 3.3K and temperature decrease by ~2° from 10 m to 79 m ASL, clearly an unstable surface layer throughout the sampled levels. This is also a weak wind case with the wind coming from the northwest. The percentage contributions of the different components are consistent at all sampled altitudes.

D. EFFECTS OF WIND AND THERMAL STABILITY

The previous individual examples indicate the impact of thermo-stability and wind speed on optical turbulence. These impacts are examined here using all available CTV measurements from CASPER-East. These results are shown in the Figures 21 and 22.

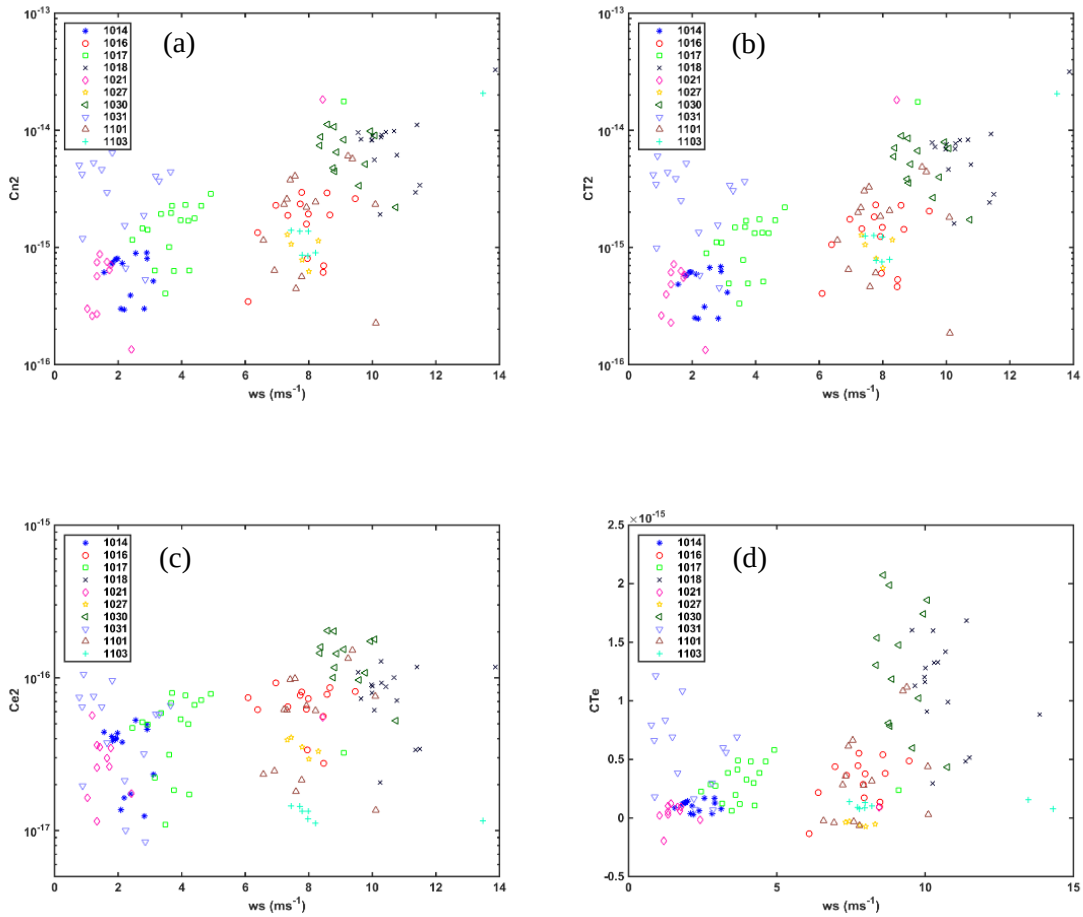

(a) C_n^2; (b) C_T^2; (c) C_e^2; and (d) C_{eT}. The horizontal axes are wind speed. Each flight was given a unique symbol and color as indicated by the legend. The four digits of the legends give month and day (MMDD) of the measurements.

Figure 21. Effects of Wind Speed on C_n^2 and its Components

The horizontal axis of Figure 21 shows the mean wind speed from each leg of all CASPER-East CTV measurements. During CASPER-East wind speed encountered were in the range between 1 ms^{-1} to about 12 ms^{-1}. Here we see C_n^2 shows an almost linear increase in the wind speed (Figure 21a). C_T^2 shows a similar trend. Although with much smaller magnitude, C_e^2 also indicates the increasing trend with wind speed. For C_{eT}, it seems to show a much stronger increase when wind speed exceeds ~6 ms^{-1}.

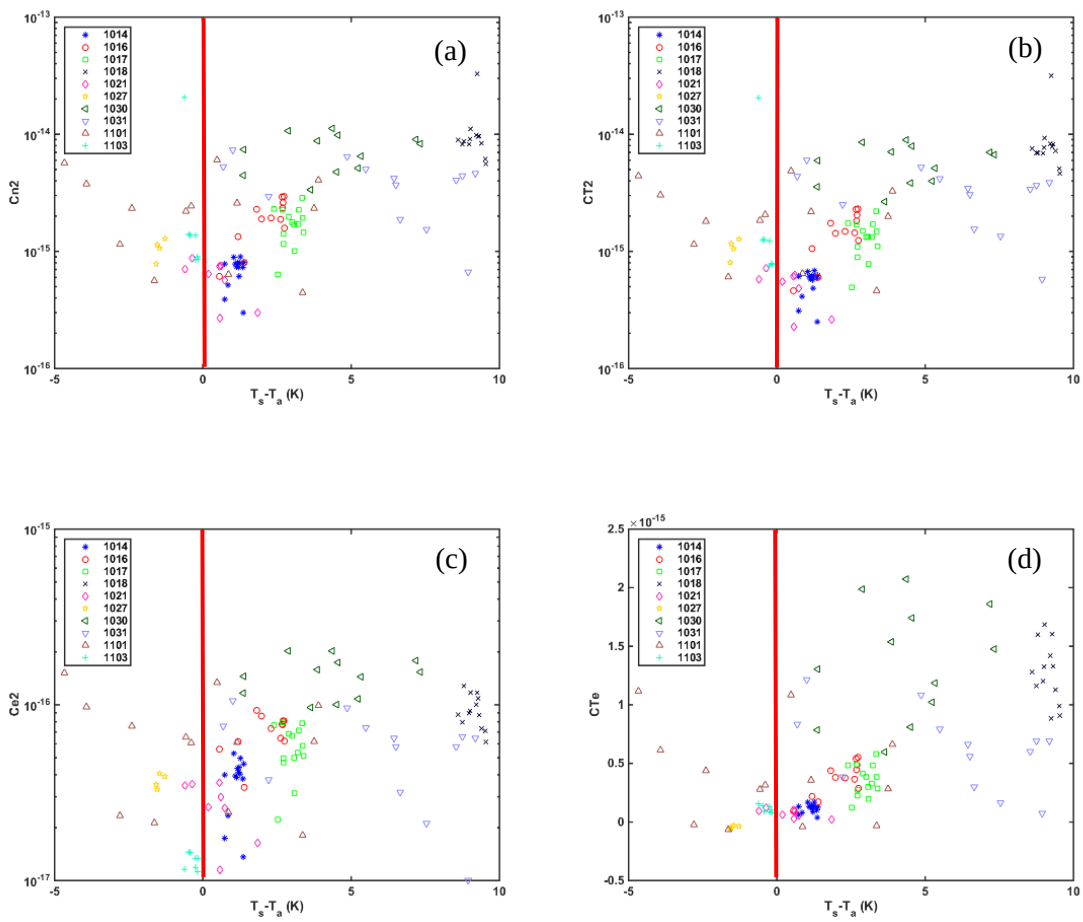

The red vertical lines separate thermal stability with stable boundary layer to the left and unstable boundary layers to the right.

Figure 22. Same as Figure 21, Except for Variation with *ASTD*

Figure 22 shows the variability of C_n^2 and its components with thermal stability (*ASTD*). In the unstable condition, there seems to be a rapid increase of C_n^2 and its components in the range when *ASTD* is less than 5°. The variation with thermal stability is less apparent in ranges of larger *ASTD*. This result seems like those indicated by the MOST theory (Frederickson 2015), although quantitative comparison in more significant details should be performed for reliable conclusions. Only a few cases of stable conditions were observed during CASPER-East, making robust conclusions in this stability regime difficult. Nevertheless, the results appear to indicate the smallest C_n^2 and all its components at neutral conditions, again a result consistent with MOST theory.

Results from 31 October are worth mentioning. This is a case with the weakest wind speed and in the precarious conditions as indicated in Figures 21 and 22. It shows the ‘unusual behavior of optical turbulence in the extreme of free convection conditions. Although this type of condition is rare over the ocean, where *ASTD*s are normally small except over the Gulf Stream. Such conditions are frequently observed overland in cloud-free conditions.

V. SUMMARY AND CONCLUSION

Advancements in conventional weapons primarily for the U. S. military is an area of special interest. Improving the Electromagnetic (EM) and Electro-Optical (EO) prediction capabilities are imperative to maintaining a tactical advantage in the operational environment. As technology evolves with the growing usage of high-energy laser systems, operating at the short-wavelength bands (i.e., LaWS). The need to understand the optical characteristics of the lower atmosphere is becoming progressively important.

The objective of this thesis work was to quantify how factors such as water vapor and temperature contributed to optical turbulence. To that end, I used data collected from CASPER-East Field Campaign CTV measurements from Twin Otter. All CTV measurements from 10 flights were analyzed 130 data legs in the lowest 50 m of the boundary layer. The focus of analyses was on C_n^2 and the component contributions, the spatial and temporal variabilities, and the physical processes affecting these quantities (wind and surface layer thermal stability). The calculations shed light on atmospheric effects that affect the propagational behaviors of optical turbulence and variables studied. Although optical turbulence was studied extensively over land, few studies focused on the marine atmospheric environment.

This research focused on the marine environment. Similarly, as with previous research over land, C_T^2 was also a major contributor to C_n^2. I further identified that the water vapor effect as C_e^2 was minimal, although its cross-correlation with temperature imposes about 20% of the total C_n^2 in the unstable conditions. A rather robust result of negative C_{eT} was found under stable conditions. The effects of cross-correlations between temperature and water vapor have previously not been studied thoroughly. I identified significant horizontal variability in C_n^2 and its components primarily related to the corresponding variability in wind speed and *ASTD*, most evident over the Gulf Stream region. This result was illustrated using individual examples as well as all data from 130 CTV level legs.

I also examined the vertical profiles of C_n^2 in the lowest 50 m and found substantial decreases with height in the marine atmospheric surface layer (MASL). This result is qualitatively consistent with those predicted by MOST. Results from all usable CTV measurements indicate a strong correlation of C_n^2 with wind speed except a case of free convection over the Gulf Stream. Stronger wind speeds enhanced C_n^2 and its components. All CTV measurements also indicate the strong impact of MASL thermo-stability on all components of C_n^2. Neutral stability has the minimum C_n^2, while C_n^2 increase with increasing magnitude of *ASTD*.

Future Work and Recommendations

Measurements by the CTV during CASPER-East provide a valuable dataset to study the characteristics of optical turbulence in the marine atmospheric boundary layer. This dataset can be further analyzed to evaluate the application of the Monin-Obukhov Similarity theory (MOST) to quantify optical turbulence. Future work should focus in this direction to best utilize this dataset to evaluate a bulk method for C_n^2 parameterization.

LIST OF REFERENCES

Alkholidi, A. and K. Altowij, 2014: Climate effects on performance of free space optical communication systems in Yemen. *Frontiers of Optoelectronics*., **7**, 91–101, https://doi.org/10.1007/s12200-014-0392-8.

Andrews, L., 2004: Field guide to atmospheric optics, *SPIE Field Guides-The International Society for Optical Engineering*, **FG02**, 1–103.

Angelo, J. A., 2009: *The facts on file: Space and Astronomy Handbook.* Infobase Publishing, 1–325.

Benito, C., A. Jiménez, C. Sánchez, and A. Navarro-Sabaté, 2012: Liquid and Solid Scintillation: Principles and Applications. *CCiTUB*, **BT.12**, 1–12, http://diposit.ub.edu/dspace/bitstream/2445/32102/1/BT12%20-%20Liquid%20and%20solid%20scintillation_ed2.pdf.

Burger, L., I.A. Litvin, and A. Forbes, 2008: Simulating atmospheric turbulence using a phase-only spatial light modulator. *Academy of Science of South Africa*., **104** 129–134, http://www.scielo.org.za/pdf/sajs/v104n3-4/a1110404.pdf.

Burk, S., 1979: Refractive Index Structure Parameter: Time-Dependent Calculating Using a Numerical Boundary-Layer Model. *J. Appl. Meteor. Climatol.*, ***19***, 562–576, http://journals.ametsoc.org/doi/abs/10.1175/1520-0450(1980)019%3C0562%3ARISPTD%3E2.0.CO%3B2.

Chu, W., 2001: The law of refraction. accessed 18 July 18, 2017, https://www.math.ubc.ca/~cass/courses/m309-01a/chu/Fundamentals/snell.htm.

Coffey, V. C., 2014: High-Energy Lasers: New Advances in Defense Applications. Optics & Photonics News*:*, accessed 06 August 2017, https://www.osa-opn.org/home/articles/volume_25/october_2014/features/high-energy_lasers_new_advances_in_defense_applica/.

Coy, S., 1999: WaveTrain: A User-Friendly Wave Optics Propagation Code. Accessed 15 June 2017, https://www.mza.com/publications/wtspiepaper.htm.

Doss-Hammel, S., E. Oh, J. Ricklin, F. Eaton, C. Gilbreath, and D. Tsintikidis, 2004: A Comparison of Optical Turbulence Models. *Proc. of SPIE*, **5550**, 236–246.

Field Research Facility, 1992: Coastal & Hydraulics Laboratory. Accessed 15 September 2017, http://frf.usace.army.mil/.

Frederickson, P. A., 2015: Further improvements and validation for the Navy Atmospheric Vertical Surface Layer Model (NAVSLaM). Paper presented at the USNC-NRSI Radio Science meeting (Joint with Ap-S Symposium), Vancouver, Canada, http://ieeexplore.ieee.org/document/7303526/.

Frehlich, R., R. Sharman, F. Vandenberghe, W. Yu, Y. Liu, J. Knievel, and G. Jumper, 2010: Estimates of C_n^2 from Numerical Weather Prediction Model Output and Comparison with Thermosonde Data. *J. Appl. Meteor. Climatol.*, **49**,1742–1755.

Hardy, J. W., 1998: *Adaptive optics for astronomical telescopes*. Oxford University Press, 1–92.

Kalogiros, J. and Q. Wang, 2011: Aircraft Observations of Sea-Surface Turbulent Fluxes Near the California Coast. *Boundary-Layer Meteorol*., **138**, 283–306, https://doi.org/10.1007/s10546-010-9585-x.

Khelif, D., 2013: Aircraft Observations for Improved Physical Parameterization for Seasonal Prediction. Department of Mechanical and Aerospace Engineering University of California, Irvine, 14 pp, https://www.onr.navy.mil/reports/FY13/mmkheli9.pdf.

Khelif, D., J. Barge, R. Yamaguchi, H. Jonsson, and Q. Wang, 2016: Controlled Towed Vehicle and Twin Otter Turbulence Measurements and Analysis. Accessed13 July 2017, https://met.nps.edu/~qwang/casper/protected/CASPER2016Review/10_Khelif_UCI_CASPER_2ndReview_2016Aug.pdf.

Khelif, D., J. Barge, R. Yamaguchi, H. Jonsson, and Q. Wang, 2017: Probing the Surface Layer over the Gulf Stream with the Controlled Towed Vehicle: Unique High-Resolution Turbulence Measurements. *Skagit 2 (Washington State Convention Center)*, https://ams.confex.com/ams/97Annual/webprogram/Paper315737.html.

Koretsky, G. J., 2013: Tutorial on Electro-Optical/Infrared (EO/IR) Theory and Systems. *Institute for Defense Analysis*, 1–100.

Lawson, J. K. and C.J. Carrano, 2006: Using Historic Models of C_n^2 to predict r0 and regimes affected by atmospheric turbulence for horizontal, slant, and topological paths. *SPIE: Optics & Photonics*, 1–14.

Lendon, B., 2014: Navy: New laser weapon works, ready for action, Accessed 16 August 2017, http://www.cnn.com/2014/12/11/tech/innovation/navy-laser-weapon.

McJannet, D. L., F.J. Cook, R. P. McGloin, H. A. McGowan, and S. Burn, 2011: Estimation of evaporation and sensible heat flux from open water. *WATER RESOURCES RESEARCH*, 1–14.

Myron B. Thompson Academy., 2006: Greenhouse Effect: Atmosphere Energy Absorption. *Climate and Water Resource Case Study:*, http://www.soest.hawaii.edu/mguidry/Unnamed_Site_2/Chapter%202/Chapter2B2.html.

Optical Sciences Company, 2011: Directed Energy Professional Society. Accessed 18 July 2017, https://protected.networkshosting.com/depsor/DEPSpages/BeamControl11ShortCourse.html#Class2.

Pedrick, A., 2004: *NASA Thesaurus*. Accessed August 5, 2017, https://www.hq.nasa.gov/office/hqlibrary/aerospacedictionary/508/s.html.

Redorbit, 2017: Scintillation. Accessed 14 June 2017, http://www.redorbit.com/reference/scintillation/.

Seeley, D. D. and J. M. Slater, 2004: High Energy Laser Joint Technology Office: A mission overview. *Proc. of SPIE*, **5552**, doi: 10.1117/12.557898; http://dx.doi.org/10.1117/12.557898.

Sprangle, P., J. Penano, and B. Hafizi, 2005: Optimum Wavelength and Power for Efficient Laser. *Naval Research Laboratory*, 1–44., www.dtic.mil/get-tr-doc/pdf?AD=ADA441474.

Sprangle, P., J. Penano, and B. Hafizi, 2007: Propagation of High Energy Laser Beams in Various Environments. *Naval Research Laboratory*, 1–55.

Tatarskii, V. I., 1971: *The Effects of the Turbulent Atmosphere on Wave Propagation.* Israel Program for Scientific Translation Ltd., 488 pp.

Thomas, F. E., 2005: The scintillation index in moderate to strong turbulence for the gaussian beam wave along a slant path. M.S. thesis, Department of Mathematics in the College of Arts and Sciences, the University of Central Florida, 77 pp., http://stars.library.ucf.edu/cgi/viewcontent.cgi?article=1507&context=etd.

Wang, Q., 2017: CASPER: Coupled Air-Sea Processes and Electromagnetic (EM) ducting Research., *Bulletin of American Meteorological Society*., 1–54.

Weidmann, D., W. J. Reburn, and K. M. Smith, 2007: Ground-based prototype quantum cascade laser heterodyne radiometer for atmospheric studies. *AIP Review of Scientific Instruments*, **78**, http://aip.scitation.org/doi/abs/10.1063/1.2753141.

Wesely, M. L., 1976: The combined effect of temperature anf humidity fluctuations on refractive index. *J. Appl. Meteor. Climatol.*, **15**, 43–49.

Wyngaard, J., and B. Kosovic, 1994: Similarity of Structure-Function Parameters in The Stably Stratified Boundary Layer. Department of Meteorology, Pennsylvania State University, **71**, 277–296.

Wyngaard, J. and D. Thomson, 1993: Refractive Index Structure in The Lower Atmosphere. Department of Meteorology, Pennsylvania State University, 34 pp.

Wyngaard, J., Y. Izumi, and S. Collins, 1971: Behavior of the Refractive-Index-Structure Parameter near the Ground. *Journal of the Optical Society of America*, **61**, 1646–1650.

Zohuri, B., 2016: Atmospheric Propagation of High-Energy Laser Beams. Accessed 16 July 2017, https://link.springer.com/chapter/10.1007/978-3-319-31289-7_8/fulltext.html.

INITIAL DISTRIBUTION LIST

1. Defense Technical Information Center
   Ft. Belvoir, Virginia

2. Dudley Knox Library
   Naval Postgraduate School
   Monterey, California